

THE SECOND *SWIFT* BURST ALERT TELESCOPE GAMMA-RAY BURST CATALOG

T. SAKAMOTO^{1,2,3}, S. D. BARTHELMY³, W. H. BAUMGARTNER^{1,2,3}, J. R. CUMMINGS^{1,2,3}, E. E. FENIMORE⁴, N. GEHRELS³,
H. A. KRIMM^{1,3,5}, C. B. MARKWARDT³, D. M. PALMER⁴, A. M. PARSONS³, G. SATO⁶, M. STAMATIKOS⁷, J. TUELLER³,
T. N. UKWATTA⁸, AND B. ZHANG⁹

¹ Center for Research and Exploration in Space Science and Technology (CREST), NASA Goddard Space Flight Center, Greenbelt, MD 20771, USA

² Joint Center for Astrophysics, University of Maryland, Baltimore County, 1000 Hilltop Circle, Baltimore, MD 21250, USA

³ NASA Goddard Space Flight Center, Greenbelt, MD 20771, USA

⁴ Los Alamos National Laboratory, P.O. Box 1663, Los Alamos, NM 87545, USA

⁵ Universities Space Research Association, 10211 Wincopin Circle, Suite 500, Columbia, MD 21044-3432, USA

⁶ Institute of Space and Astronautical Science, JAXA, Kanagawa 229-8510, Japan

⁷ Center for Cosmology and Astro-Particle Physics, Department of Physics, The Ohio State University, 191 West Woodruff Avenue, Columbus, OH 43210, USA

⁸ Department of Physics and Astronomy, Michigan State University, 3245 BPS Building, East Lansing, MI 48824, USA

⁹ Department of Physics and Astronomy, University of Nevada, Las Vegas, NV 89154, USA

Received 2010 June 26; accepted 2011 April 18; published 2011 June 15

ABSTRACT

We present the second *Swift* Burst Alert Telescope (BAT) catalog of gamma-ray bursts (GRBs), which contains 476 bursts detected by the BAT between 2004 December 19 and 2009 December 21. This catalog (hereafter the BAT2 catalog) presents burst trigger time, location, 90% error radius, duration, fluence, peak flux, time-averaged spectral parameters, and time-resolved spectral parameters measured by the BAT. In the correlation study of various observed parameters extracted from the BAT prompt emission data, we distinguish among long-duration GRBs (L-GRBs), short-duration GRBs (S-GRBs), and short-duration GRBs with extended emission (S-GRBs with E.E.) to investigate differences in the prompt emission properties. The fraction of L-GRBs, S-GRBs, and S-GRBs with E.E. in the catalog are 89%, 8%, and 2%, respectively. We compare the BAT prompt emission properties with the BATSE, *BeppoSAX*, and *HETE-2* GRB samples. We also correlate the observed prompt emission properties with the redshifts for the GRBs with known redshift. The BAT T_{90} and T_{50} durations peak at 70 s and 30 s, respectively. We confirm that the spectra of the BAT S-GRBs are generally harder than those of the L-GRBs. The time-averaged spectra of the BAT S-GRBs with E.E. are similar to those of the L-GRBs. Whereas, the spectra of the initial short spikes of the S-GRBs with E.E. are similar to those of the S-GRBs. We show that the BAT GRB samples are significantly softer than the BATSE bright GRBs and that the time-averaged $E_{\text{peak}}^{\text{obs}}$ of the BAT GRBs peaks at 80 keV, which is significantly lower energy than those of the BATSE sample, which peak at 320 keV. The time-averaged spectral properties of the BAT GRB sample are similar to those of the *HETE-2* GRB samples. By time-resolved spectral analysis, we find that only 10% of the BAT observed photon indices are outside the allowed region of the synchrotron shock model. We see no obvious observed trend in the BAT T_{90} and the observed spectra with redshifts. The T_{90} and T_{50} distributions measured at the 140–220 keV band in the GRB rest frame from the BAT known redshift GRBs peak at 19 s and 8 s, respectively. We also provide an update on the status of the on-orbit BAT calibrations.

Key words: gamma-ray burst: general

Online-only material: color figures, machine-readable tables

1. INTRODUCTION

The *Swift* mission (Gehrels et al. 2004) has revolutionized our understanding of gamma-ray bursts (GRBs) and their usage to study the early universe with the sophisticated on-board localization capability of the *Swift* Burst Alert Telescope (BAT; Barthelmy et al. 2005a). The autonomous spacecraft slews to point the X-Ray Telescope (XRT; Burrows et al. 2005) and the UV/Optical Telescope (UVOT; Roming et al. 2005) to the GRB location to start an immediate follow-up observation. The precise GRB location provided by *Swift* permits coordinated multi-wavelength observations on the ground. Since the release of the first BAT GRB catalog (Sakamoto et al. 2008), there have been more notable discoveries. On 2009 April 23, *Swift* BAT detected GRB 090423 at a redshift of 8.2. This implies that massive stars were produced about 630 Myr after the big bang (Tanvir et al. 2009; Salvaterra et al. 2009). In GRB 080319B, extraordinary, bright, variable optical emission, which peaked at the visual magnitude of 5.3, has been observed while the prompt gamma-ray emission was still active. This observation

suggests for the first time that there can exist a prompt optical emission component that tracks the gamma-ray light curve but belongs to a different spectral component (Racusin et al. 2008). *Swift* has been increasing the number of identifications of host galaxies for short-duration bursts. Based on the *Swift* sample, we are observing a wide variety of burst characteristics (e.g., Berger 2009). Furthermore, progress is being made in studying the properties of host galaxies of dark bursts, allowing us to understand the differences in the birth places of dark GRBs, as compared to the hosts of GRBs with bright optical afterglows (e.g., Perley et al. 2009).

The first BAT GRB catalog (the BAT1 catalog; Sakamoto et al. 2008) consisted of 237 bursts from 2004 December 19 to 2007 June 16. The BAT1 catalog contained burst trigger time, location, 90% error radius, duration, fluence, peak flux, and time-averaged spectral parameters. Here we present the second BAT GRB catalog (the BAT2 catalog), including 476 GRBs detected by BAT from 2004 December 19 to 2009 December 21. The GRB samples in the BAT1 catalog have been re-analyzed by the latest BAT software and calibration files. In addition to

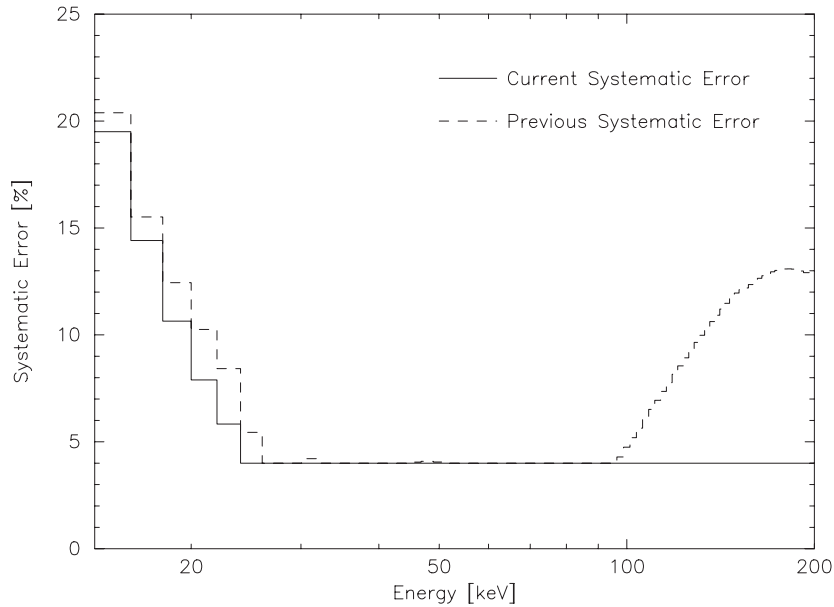


Figure 1. Systematic error as a function of energy. The current systematic error is shown in a solid line and the previous systematic error (used in the analysis of the BAT1 catalog) is shown in a dashed line.

the parameters in the BAT1 catalog, the BAT2 catalog includes time-resolved spectral parameters. The catalog also presents correlations between the prompt emission properties of known redshift GRBs.

In Section 2, we summarize the updates to the in-orbit calibration of the BAT instrument. In Section 3, we describe the analysis methods used in compiling the catalog. In Section 4, we describe the content of the tables in the catalog and show the prompt emission properties of the BAT GRBs from the catalog. Our conclusions are summarized in Section 5. All quoted errors in this work are at the 90% confidence level.

2. UPDATES TO IN-ORBIT CALIBRATIONS

The BAT is a highly sensitive, large field of view (FOV; 2.2 sr for $>10\%$ coded FOV), coded-aperture telescope that detects and localizes GRBs in real time. The BAT detector plane is composed of 32,768 pieces of CdZnTe (CZT: $4 \times 4 \times 2$ mm), and the coded-aperture mask is composed of $\sim 52,000$ lead tiles ($5 \times 5 \times 1$ mm) with a 1 m separation between mask and detector plane. The energy range is 14–150 keV for imaging, which is a technique to subtract the background based on the modulation resulting from the coded mask, and spectra can be obtained with no position information up to 350 keV. Further detailed descriptions and references of the BAT instrument can be found in the BAT1 GRB catalog.

There have been two major updates to the energy calibration of the BAT since the publication of the BAT1 catalog. The first update is the identification of a problem in the energy response above 100 keV. The mobility-lifetime products of electrons and holes ($\mu\tau$) which are used to model the energy response of an individual CZT detector (Sato et al. 2005; Suzuki et al. 2005) are found to be 1.7 times larger than those originally determined in the ground calibration. This fix eliminates the ad hoc correction formerly applied above 100 keV to reproduce the assumed photon index and flux values based on the Crab spectrum (see below) and also reduces the level of systematic errors (see Figure 1). These changes in the energy response and

the systematic error are available to the public (BAT CALDB 20081026).

The second update is a correction to the measured gain of the detectors. An analysis of four years of on-board ^{241}Am spectra shows a shift of 2.5 keV in the position of the 59.5 keV line. The BAT team has developed new calibration files (coefficients to convert from the pulse height analyzer (PHA) channel to energy) to correct this gain change as a function of time. After applying the new gain correction, the scatter of the 59.5 keV line energy is ~ 0.1 keV over the four-year period. The calibration file to correct this time-dependent gain change will be released to the public in summer of 2011.

Figure 2 shows the Crab photon index and the flux in the 15–150 keV band as a function of incident angle using the latest BAT software and calibration files. Both the photon index and the flux are within $\pm 5\%$ and $\pm 10\%$, respectively, of the assumed Crab values¹⁰ based on Rothschild et al. (1998) and Jung (1989) over the BAT FOV. The deviation of the derived parameters from the Crab canonical values is larger toward the edge of the BAT FOV. Therefore, a larger systematic error in the spectral parameters could exist if the source is located at the edge of the field of BAT. We also note that the photon index is systematically harder by ~ 0.02 than the Crab canonical value of -2.15 for observations with $\theta < 10^\circ$.

3. ANALYSIS FOR THE GRB CATALOG

We used standard BAT software (HEASOFT 6.8) and the latest calibration database to process the BAT GRBs from 2004 December (GRB 041217) to 2009 December (GRB 091221). The various data types of the BAT instrument are described in details in Barthelmy et al. (2005a). The GRBs included in the BAT1 catalog have been reprocessed. The BAT2 catalog sample also includes bursts which did not trigger BAT in flight, but were found in ground processing. The burst pipeline script, `batgrbproduct`, was used to process the BAT event data. Since the burst emission is longer than the interval during which the

¹⁰ The assumed Crab values in the BAT energy range are -2.15 for the photon index and 2.11×10^{-8} erg cm $^{-2}$ s $^{-1}$ for the flux in the 15–150 keV band.

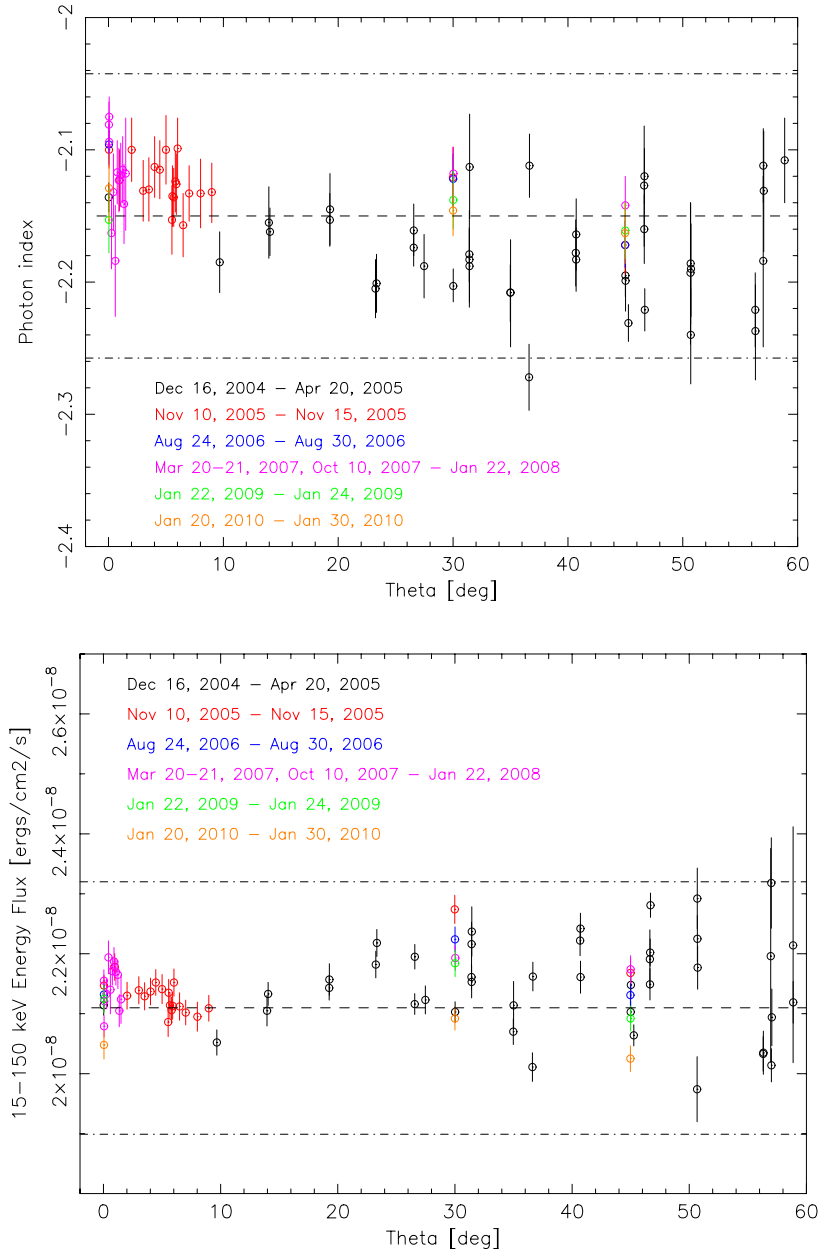


Figure 2. Power-law photon index (top) and the flux in the 15–150 keV band as a function of the incident angle of the Crab observed in different time periods. The horizontal dashed lines are the Crab canonical values of -2.15 for the photon index and $2.11 \times 10^{-8} \text{ erg cm}^{-2} \text{ s}^{-1}$ for the flux. The dash-dotted lines are $\pm 5\%$ of the photon index and $\pm 10\%$ of the flux canonical values.

(A color version of this figure is available in the online journal.)

instrument collected data in event mode for GRB 060124 and GRB 060218, we used both event data and survey data (Detector Plane Histogram data) to calculate the fluence and the time-averaged spectral parameters. We used raw light curve data (quad-rate data) to measure the durations of most of the bursts found in ground processing because the event data do not cover the whole burst episode for these bursts. For most bursts we use `battblocks`, one of the tasks run in `batgrbproduct`, to determine the burst duration using the Bayesian block algorithm (Scargle 1998).¹¹ For some bursts `battblocks` failed to find a

valid burst interval. In these cases, we fitted the light curve with background subtracted using the modulation resulting from the coded mask (a called mask-weighted light curve) over the full BAT energy range. We applied a linear-rise, exponential decay model (“BURS” model in `ftools qdp`¹²) to find the burst time intervals (T_{100} , T_{90} , T_{50} , and peak 1 s intervals) and created the T_{100} and peak 1 s PHA files (80 channels) based on these time intervals. We include comments in Table 1 for the bursts which have anomalies either in the data or the processing.

For the time-averaged spectral analysis, we used the time interval from the emission start time to the emission end time (T_{100} interval) which is determined by Bayesian-block technique (`battblocks`). For many bursts, the spacecraft slew for the XRT and UVOT pointing occurred while the prompt

¹¹ `batgrbproduct` calls `battblocks` using, in turn, mask-weighted light curves with bin widths 4 ms, 16 ms, 1 s, and 16 s to measure T_{90} and T_{50} durations. It then applies a set of criteria starting with the shortest bin size to decide whether or not to accept a duration estimate. If a measured duration is greater than two times the bin size, and 30% greater than the previous best estimate, then the current estimate becomes the new best estimate.

¹² <http://heasarc.gsfc.nasa.gov/docs/software/ftools/others/qdp/qdp.html>

Table 1
BAT GRB Summary

| GRB Name | Trigger Number | Trigger Time | R.A. (°) | Decl. (°) | R.A.(XRT) (°) | Decl.(XRT) (°) | SN _{img} (σ) | Error (′) | T ₉₀ (s) | T ₅₀ (s) | Start (s) | Stop (s) | Note |
|----------|----------------|--------------------------|----------|-----------|---------------|----------------|-----------------------|-----------|---------------------|---------------------|-----------|----------|------|
| 041217 | 100116 | 2004 Dec 17 07:28:25.920 | 164.790 | −17.944 | ... | ... | 19.3 | 1.4 | 5.65 | 2.71 | −2 | 18 | |
| 041219A | 100318 | 2004 Dec 19 01:42:18.000 | 6.154 | 62.847 | ... | ... | ... | ... | ... | ... | ... | ... | (1) |
| 041219B | 100367 | 2004 Dec 19 15:38:48.000 | 167.674 | −33.458 | ... | ... | ... | ... | ... | ... | ... | ... | (1) |
| 041219C | 100380 | 2004 Dec 19 20:30:34.000 | 343.882 | −76.786 | ... | ... | 13.2 | 1.8 | 10.00 | 4.00 | −3 | 17 | |
| 041220 | 100433 | 2004 Dec 20 22:58:26.599 | 291.301 | 60.596 | ... | ... | 31.9 | 1.0 | 5.58 | 2.20 | −300 | 302 | |
| 041223 | 100585 | 2004 Dec 23 14:06:17.956 | 100.186 | −37.072 | ... | ... | 83.7 | 1.0 | 109.08 | 29.20 | −299 | 303 | |
| 041224 | 100703 | 2004 Dec 24 20:20:57.698 | 56.192 | −6.666 | ... | ... | 11.4 | 2.0 | 177.17 | 37.68 | −299 | 303 | |
| 041226 | 100815 | 2004 Dec 26 20:34:18.976 | 79.647 | 73.343 | ... | ... | 5.6 | 3.3 | 89.50 | 52.72 | −299 | 303 | (11) |
| 041228 | 100970 | 2004 Dec 28 10:49:14.142 | 336.649 | 5.027 | ... | ... | 36.5 | 1.0 | 52.16 | 19.54 | −299 | 303 | |
| 050117 | 102861 | 2005 Jan 17 12:52:36.037 | 358.490 | 65.934 | ... | ... | 53.8 | 1.0 | 166.65 | 83.51 | −299 | 303 | |

Notes.

- ¹ The event data are not available.
- ² Short-duration GRB.
- ³ The event data of the part of the burst emission are not available.
- ⁴ Short-duration GRB with an extended emission.
- ⁵ Battblocks failed because of the weak nature of the burst.
- ⁶ GRB found by the ground process.
- ⁷ The detector plane histogram data are used in the fluence calculation and the spectral analysis.
- ⁸ Possible GRB.
- ⁹ GRB found by the BAT slew survey process.
- ¹⁰ T₉₀ and T₅₀ are lower limit.
- ¹¹ Re-calculate the image significance using the interval determined by the flight software.

(This table is available in its entirety in a machine-readable form in the online journal. A portion is shown here for guidance regarding its form and content.)

emission was ongoing. This creates a complication for the derivation of the spectral response since the BAT energy response generator, `batdrmggen`, can only produce a response at a single fixed incident angle of the source. To find a response during a slew, we created detector energy response matrices (DRMs) for each five-second period during the time T_{100} interval, taking into account the changing position of the GRB in detector coordinates especially during the spacecraft slew. We then weighted these DRMs by the five-second count rates and created an averaged DRM using `addrmf`. The count-weighted BAT DRMs have been tested on a subset of GRBs which were simultaneously detected by the *Konus-Wind* and the *Suzaku* Wide-band All-sky Monitor instruments. The joint spectral analysis using the weighted BAT DRM for the jointly detected GRBs shows no systematic trend in the BAT-derived parameters compared to the spectral parameters derived by other GRB instruments (Sakamoto et al. 2011).

We extracted time-resolved spectra for the relevant intervals determined with `battblocks`. Since the first and the last intervals identified by `battblocks` are the pre- and post-burst backgrounds, the spectrum for these two intervals was not created. For the time-resolved spectral analysis, we created a DRM for each spectrum by taking into account the GRB position in detector coordinates and updating the keywords of the spectral files using `batupdatephakw` before running `batdrmggen` to generate the DRM. We also created individual DRMs for the peak spectra used to calculate the peak flux (see below).

The spectra were fitted with a simple power-law (PL) model,

$$f(E) = K_{50}^{\text{PL}} \left(\frac{E}{50 \text{ keV}} \right)^{\alpha^{\text{PL}}}, \quad (1)$$

where α^{PL} is the PL photon index and K_{50}^{PL} is the normalization at 50 keV in units of photons $\text{cm}^{-2} \text{s}^{-1} \text{keV}^{-1}$. We also used a

cutoff power-law (CPL) model,

$$f(E) = K_{50}^{\text{CPL}} \left(\frac{E}{50 \text{ keV}} \right)^{\alpha^{\text{CPL}}} \exp \left(\frac{-E(2 + \alpha^{\text{CPL}})}{E_{\text{peak}}} \right), \quad (2)$$

where α^{CPL} is the PL photon index, E_{peak} is the peak energy in the νF_{ν} spectrum, and K_{50}^{CPL} is the normalization at 50 keV in units of photons $\text{cm}^{-2} \text{s}^{-1} \text{keV}^{-1}$. All of the BAT spectra are acceptably fit by either a PL or a CPL model. The same criterion as in the BAT1 catalog, $\Delta\chi^2$ between a PL and a CPL fit greater than 6 ($\Delta\chi^2 \equiv \chi_{\text{PL}}^2 - \chi_{\text{CPL}}^2 > 6$), was used to determine if the CPL model is a better spectral model for the data. Note that none of the BAT spectra show a significant improvement in χ^2 with a Band function (Band et al. 1993) fit compared to that of a CPL model fit.

The fluence, the 1 s, and the 20 ms peak fluxes were derived from the spectral fits. The fluences were calculated by fitting the time-averaged spectrum with the best-fit spectral model. The 1 s and 20 ms peak fluxes were calculated by fitting the spectrum of the 1 s and the 20 ms interval bracketing the highest peak in the light curve. Those intervals were identified by `battblocks`. Similarly, we used the best-fit spectral model to calculate the peak fluxes. Since the shortest burst duration observed by BAT is around 20 ms, we chose this window size to measure the peak flux on the shortest timescale. Note that since the total number of photons for a 20 ms spectrum is generally small, we created a spectrum in 10 logarithmically spaced channels from 14 keV to 150 keV to use for the fit. We are not always able to report a 20 ms peak flux. For 29 GRBs, an unexplained systematic effect leads to an unacceptable reduced χ^2 ($\chi_{\nu}^2 > 2$) in both the PL and CPL fit. Furthermore, for 31 GRBs we could not create the 20 ms peak spectrum because `battblocks` failed to find the interval.

For GRBs with known redshift, we calculated the T_{90} and T_{50} durations in the 140–220 keV band in the GRB rest frame. By fixing the energy range in the GRB rest frame, there is no

Table 2
BAT GRB Energy Fluence

| GRB Name | Spectral Model | S (15–25) | S (25–50) | S (50–100) (10^{-8} erg cm^{-2}) | S (100–150) | S (15–150) | Start (s) | Stop (s) | Note |
|----------|----------------|------------------|------------------|--|------------------|-------------------|-----------|----------|------|
| 041217 | CPL | 30.0 ± 3.1 | 72.1 ± 3.3 | 106.0 ± 5.3 | 61.1 ± 8.1 | 270.0 ± 12.1 | +0.82 | +7.89 | |
| 041219A | ... | ... | ... | ... | ... | ... | ... | ... | (1) |
| 041219B | ... | ... | ... | ... | ... | ... | ... | ... | (1) |
| 041219C | PL | 25.5 ± 2.0 | 34.5 ± 1.6 | 34.4 ± 2.5 | 20.0 ± 2.3 | 114.0 ± 5.8 | +0.00 | +12.00 | |
| 041220 | PL | 5.9 ± 0.6 | 9.8 ± 0.7 | 12.3 ± 1.2 | 8.6 ± 1.3 | 36.6 ± 2.8 | -0.21 | +6.81 | |
| 041223 | PL | 153.0 ± 5.8 | 347.0 ± 7.7 | 624.0 ± 10.4 | 576.0 ± 15.3 | 1700.0 ± 27.2 | -10.54 | +145.94 | |
| 041224 | CPL | 133.0 ± 11.0 | 261.0 ± 10.4 | 309.0 ± 14.2 | 149.0 ± 21.1 | 853.0 ± 34.3 | -109.63 | +116.27 | |
| 041226 | PL | 3.8 ± 1.5 | 7.4 ± 1.8 | 11.0 ± 3.4 | 8.9 ± 4.3 | 31.0 ± 8.2 | -1.34 | +93.50 | |
| 041228 | PL | 52.8 ± 4.2 | 90.2 ± 4.2 | 118.0 ± 6.1 | 84.7 ± 7.1 | 345.0 ± 14.8 | -0.40 | +66.78 | |
| 050117 | CPL | 112.0 ± 7.1 | 226.0 ± 5.9 | 318.0 ± 9.2 | 211.0 ± 15.6 | 867.0 ± 23.0 | +4.28 | +215.86 | |

Notes.¹ The event data are not available.² The event data of the part of the burst emission are not available.³ S (100–150) is an upper limit.⁴ S (50–100) is an upper limit.

(This table is available in its entirety in a machine-readable form in the online journal. A portion is shown here for guidance regarding its form and content.)

need to apply a correction to the measured duration because of the difference in the GRB width as a function of the observed energy band (e.g., Fenimore et al. 1995). We created the light curves in the energy range $140/(1+z)$ keV to $220/(1+z)$ keV with `batbinevt`. This energy band was chosen so that the redshift of the nearest GRB $z = 0.1257$ (GRB 060614) constrains the upper boundary: $220 \text{ keV}/(1+0.1257) = 195 \text{ keV}$, and the most distant GRB $z = 8.26$ (GRB 090423) constrains the lower boundary: $140 \text{ keV}/(1+8.26) = 15 \text{ keV}$, where 15–195 keV is the BAT observed energy range. We used the same algorithm in `batgrbproduct` to find the best T_{90} and T_{50} durations in the observed $140/(1+z)$ – $220/(1+z)$ keV band. We then divided the duration by $(1+z)$ to correct for the time-dilation effect due to cosmic expansion.

4. THE CATALOG

The BAT2 catalog includes GRBs detected by BAT in five years of operation between 2004 December 19 and 2009 December 31. The 476 GRBs in the catalog include 25 GRBs found in ground processing (eight of the 25 were found by the BAT slew survey; Copete et al. 2007) and four possible GRBs. The definition of a possible GRB is an event for which the BAT image significance based on the ground analysis is less than 6σ and there is no XRT X-ray counterpart. The first column of Table 1 is the GRB name. The next column is the BAT trigger number. The next column specifies the BAT trigger time in UTC in the form of *YYYY-MM-DD hh:mm:ss.sss* where *YYYY* is year, *MM* month, *DD* day of month, *hh* hour, *mm* minute, and *ss.sss* second. Note that the definition of the BAT trigger time is the start time of the image from which the GRB is detected on-board. The next six columns give, respectively, the location derived in ground processing for BAT¹³ and XRT in equatorial (J2000) coordinates, the signal-to-noise ratio (S/N) of the BAT image at that location, and the radius of the 90% confidence

region in arcminutes. The 90% error radius is calculated based on the S/N of the image using the following equation derived from the BAT hard X-ray survey process:¹⁴

$$r_{90\%} = 10.92 \times \text{S/N}^{-0.7} \text{ (arcmin)},$$

where S/N is the signal-to-noise ratio of the GRB point source in BAT image. However, due to limitations in our knowledge of the BAT point-spread function, we quote the minimum allowed value of $r_{90\%}$ as $1'$ in the catalog. The next two columns specify the burst durations which contain from 5% to 95% (T_{90}) and from 25% to 75% (T_{50}) of the total burst fluence. These durations are calculated in the 15–350 keV band.¹⁵ The next two columns are the start and stop times measured from the BAT trigger time of the available event data. The last column contains the comments.

The energy fluences calculated in various energy bands are summarized in Table 2. The first column is the GRB name. The next column specifies the spectral model which was used in deriving the fluences (PL: simple power-law model; Equation (1), CPL: cutoff power-law model; Equation (2)). The next five columns are the fluences in the 15–25 keV, 25–50 keV, 50–100 keV, 100–150 keV, and 15–150 keV bands. The unit of fluence is 10^{-8} erg cm^{-2} . The next two columns specify the start and stop times relative to the BAT trigger time of the interval used to calculate the fluences. The last column contains the comments. Note that fluences are not reported for GRBs with incomplete data.

Tables 3 and 4 summarize the 1 s peak photon and energy fluxes, respectively, in various energy bands. The first column is the GRB name. The next column specifies the spectral model used in deriving the 1 s peak flux. The next five columns are the peak photon and energy fluxes in the 15–25 keV, 25–50 keV, 50–100 keV, 100–150 keV, and 15–150 keV bands. The unit of the flux is photons $\text{cm}^{-2} \text{ s}^{-1}$ for the peak photon flux and 10^{-8} erg $\text{cm}^{-2} \text{ s}^{-1}$ for the peak energy flux. The penultimate column in Table 3 specifies the start time relative to the BAT

¹³ `batgrbproduct` creates a BAT sky image in the 15–350 keV band using event data from before the autonomous spacecraft slew to a GRB location. The foreground and background intervals used to create the image are determined by `battblocks`. If `battblocks` failed to find the intervals, `batgrbproduct` uses the same intervals identified by the BAT on-board software. The tool `batcelldetect` is used to find the GRB location in the background subtracted image.

¹⁴ http://heasarc.gsfc.nasa.gov/docs/swift/analysis/bat_digest.html

¹⁵ The coded mask is transparent to photons above 150 keV. Thus, photons above 150 keV are treated as background in the mask-weighted method. The effective upper boundary is thus ~ 150 keV.

Table 3
BAT GRB 1 s Peak Photon Flux

| GRB Name | Spectral Model | $F_{\text{photon}}^{\text{P}}(15-25)$ | $F_{\text{photon}}^{\text{P}}(25-50)$ | $F_{\text{photon}}^{\text{P}}(50-100)$ (photons $\text{cm}^{-2} \text{s}^{-1}$) | $F_{\text{photon}}^{\text{P}}(100-150)$ | $F_{\text{ph}}^{\text{P}}(15-150)$ | Start (s) | Note |
|----------|----------------|---------------------------------------|---------------------------------------|---|---|------------------------------------|-----------|------|
| 041217 | PL | 2.09 ± 0.25 | 2.24 ± 0.17 | 1.70 ± 0.14 | 0.796 ± 0.106 | 6.82 ± 0.48 | +3.26 | |
| 041219A | ... | ... | ... | ... | ... | ... | ... | (1) |
| 041219B | ... | ... | ... | ... | ... | ... | ... | (1) |
| 041219C | PL | 0.88 ± 0.14 | 0.78 ± 0.04 | 0.48 ± 0.03 | 0.19 ± 0.02 | 2.33 ± 0.23 | +2.00 | |
| 041220 | PL | 0.52 ± 0.03 | 0.58 ± 0.02 | 0.46 ± 0.02 | 0.22 ± 0.02 | 1.78 ± 0.13 | -0.02 | |
| 041223 | PL | 1.51 ± 0.11 | 2.20 ± 0.10 | 2.38 ± 0.10 | 1.48 ± 0.05 | 7.58 ± 0.29 | +35.01 | |
| 041224 | PL | 0.82 ± 0.14 | 0.95 ± 0.10 | 0.79 ± 0.04 | 0.40 ± 0.03 | 2.95 ± 0.29 | -0.06 | |
| 041226 | PL | 0.09 ± 0.02 | 0.11 ± 0.02 | 0.09 ± 0.02 | 0.05 ± 0.01 | 0.34 ± 0.05 | +3.31 | |
| 041228 | PL | 0.63 ± 0.15 | 0.56 ± 0.04 | 0.34 ± 0.03 | 0.13 ± 0.02 | 1.65 ± 0.24 | +22.03 | |
| 050117 | PL | 0.51 ± 0.03 | 0.70 ± 0.03 | 0.70 ± 0.03 | 0.41 ± 0.03 | 2.32 ± 0.16 | +87.22 | |

Notes.¹ The event data are not available.² The event data of the part of the burst emission are not available.³ $F_{\text{photon}}^{\text{P}}(15-25)$ is an upper limit.⁴ $F_{\text{photon}}^{\text{P}}(25-50)$ is an upper limit.⁵ $F_{\text{photon}}^{\text{P}}(50-100)$ is an upper limit.⁶ $F_{\text{photon}}^{\text{P}}(100-150)$ is an upper limit.⁷ $F_{\text{photon}}^{\text{P}}(15-150)$ is an upper limit.

(This table is available in its entirety in a machine-readable form in the online journal. A portion is shown here for guidance regarding its form and content.)

Table 4
BAT GRB 1 s Peak Energy Flux

| GRB Name | Spectral Model | $F_{\text{ene}}^{\text{P}}(15-25)$ | $F_{\text{ene}}^{\text{P}}(25-50)$ | $F_{\text{ene}}^{\text{P}}(50-100)$ ($10^{-8} \text{ erg cm}^{-2} \text{ s}^{-1}$) | $F_{\text{ene}}^{\text{P}}(100-150)$ | $F_{\text{ene}}^{\text{P}}(15-150)$ | Note |
|----------|----------------|------------------------------------|------------------------------------|---|--------------------------------------|-------------------------------------|------|
| 041217 | PL | 6.5 ± 0.8 | 12.7 ± 0.9 | 19.3 ± 1.7 | 15.7 ± 2.1 | 54.2 ± 4.2 | |
| 041219A | ... | ... | ... | ... | ... | ... | (1) |
| 041219B | ... | ... | ... | ... | ... | ... | (1) |
| 041219C | PL | 2.7 ± 0.4 | 4.4 ± 0.4 | 5.4 ± 0.7 | 3.7 ± 0.8 | 16.3 ± 1.8 | |
| 041220 | PL | 1.6 ± 0.2 | 3.3 ± 0.3 | 5.2 ± 0.5 | 4.4 ± 0.7 | 14.5 ± 1.3 | |
| 041223 | PL | 4.8 ± 0.4 | 12.8 ± 0.6 | 27.7 ± 1.2 | 29.4 ± 1.9 | 74.6 ± 3.2 | |
| 041224 | PL | 2.5 ± 0.4 | 5.4 ± 0.6 | 9.0 ± 1.0 | 7.9 ± 1.3 | 24.9 ± 2.6 | |
| 041226 | PL | 0.3 ± 0.1 | 0.6 ± 0.2 | 1.1 ± 0.4 | 1.0 ± 0.5 | 2.9 ± 0.9 | |
| 041228 | PL | 2.0 ± 0.5 | 3.1 ± 0.5 | 3.8 ± 0.8 | 2.6 ± 0.8 | 11.4 ± 1.8 | |
| 050117 | PL | 1.6 ± 0.2 | 4.0 ± 0.3 | 8.1 ± 0.6 | 8.2 ± 1.0 | 21.9 ± 1.7 | |

Notes.¹ The event data are not available.² The event data of the part of the burst emission are not available.³ $F_{\text{ene}}^{\text{P}}(15-25)$ is an upper limit.⁴ $F_{\text{ene}}^{\text{P}}(25-50)$ is an upper limit.⁵ $F_{\text{ene}}^{\text{P}}(50-100)$ is an upper limit.⁶ $F_{\text{ene}}^{\text{P}}(100-150)$ is an upper limit.⁷ $F_{\text{ene}}^{\text{P}}(15-150)$ is an upper limit.

(This table is available in its entirety in a machine-readable form in the online journal. A portion is shown here for guidance regarding its form and content.)

trigger time for the peak second. The last column contains the comments.

Table 5 shows the 20 ms peak energy and photon flux in the 15–150 keV band. The first column is the GRB name. The next column shows the spectral model used in deriving the flux. The next two columns are the peak energy flux and photon flux in the 15–150 keV band. The unit of the flux is photons $\text{cm}^{-2} \text{s}^{-1}$ for the peak photon flux and $10^{-8} \text{ erg cm}^{-2} \text{s}^{-1}$ for the peak energy flux. The next column specifies the start time relative to the BAT trigger time for the 20 ms peak. The last column contains the comments.

The time-averaged spectral parameters are listed in Table 6. The first column is the GRB name. The next three columns

are the photon index, the normalization at 50 keV in units of $10^{-4} \text{ photons cm}^{-2} \text{s}^{-1} \text{keV}^{-1}$, and χ^2 of the fit for a PL model. The next four columns are the photon index, $E_{\text{peak}}^{\text{obs}}$ in units of keV, the normalization at 50 keV in units of $10^{-3} \text{ photons cm}^{-2} \text{s}^{-1} \text{keV}^{-1}$ and χ^2 of the fit in a CPL model. The spectral parameters in a CPL are only shown for the bursts which meet the criteria described in Section 3. The number of degrees of freedom is 57 for a PL fit and 56 for a CPL fit except for GRB 060124 and GRB 060218 (see the comment column of the table). The last column contains the comments.

The time-resolved spectral parameters are listed in Table 7. The total number of time-resolved spectra is 3323. The first column is the GRB name. The next two columns specify the

Table 5
BAT GRB 20 ms Peak Photon and Energy Flux

| GRB Name | Spectral Model | $F_{\text{ene}}^{\text{P}}(15-150)$ ($10^{-8} \text{ erg cm}^{-2} \text{ s}^{-1}$) | $F_{\text{photon}}^{\text{P}}(15-150)$ (photons $\text{cm}^{-2} \text{ s}^{-1}$) | Start (s) | Note |
|----------|----------------|---|--|-----------|------|
| 041217 | CPL | 75.5 ± 31.0 | 9.5 ± 3.3 | +3.63 | |
| 041219A | ... | ... | ... | ... | (1) |
| 041219B | ... | ... | ... | ... | (1) |
| 041219C | PL | 20.8 ± 10.8 | 4.1 ± 1.6 | +8.13 | |
| 041220 | PL | 33.0 ± 11.8 | 3.1 ± 1.0 | +0.25 | |
| 041223 | PL | 124.0 ± 27.1 | 11.3 ± 2.2 | +24.30 | |
| 041224 | CPL | 44.6 ± 18.5 | 5.9 ± 2.1 | +0.68 | |
| 041226 | PL | 13.1 ± 7.1 | 1.4 ± 0.7 | +2.75 | |
| 041228 | ... | ... | ... | +2.49 | (2) |
| 050117 | CPL | 41.9 ± 16.6 | 4.0 ± 1.2 | +88.02 | |

Notes.¹ The event data are not available.² Reduced χ^2 is greater than 2.³ The event data of the part of the burst emission are not available.⁴ $F_{\text{ene}}^{\text{P}}(15-150)$ is an upper limit.⁵ $F_{\text{photon}}^{\text{P}}(15-150)$ is an upper limit.⁶ Battblocks failed because of the weak nature of the burst.

(This table is available in its entirety in a machine-readable form in the online journal. A portion is shown here for guidance regarding its form and content.)

start and the stop time relative to the BAT trigger time of the interval used to extract the spectrum. The next four columns are the photon index, the normalization at 50 keV in units of 10^{-4} photons $\text{cm}^{-2} \text{ s}^{-1} \text{ keV}^{-1}$, χ^2 of the fit for a PL model, and the energy flux in the 15–150 keV band in units of $10^{-8} \text{ erg cm}^{-2} \text{ s}^{-1}$. The next five columns are the photon index, $E_{\text{peak}}^{\text{obs}}$ in units of keV, the normalization at 50 keV in units of 10^{-3} photons $\text{cm}^{-2} \text{ s}^{-1} \text{ keV}^{-1}$, χ^2 of the fit in a CPL model, and the energy flux in units of $10^{-8} \text{ erg cm}^{-2} \text{ s}^{-1}$. The

last column contains the comment. As in Table 6, we only show CPL parameters for the fits which meet our $\Delta\chi^2$ criteria.

Table 8 shows the T_{90} and T_{50} durations measured in the 140–220 keV band in the GRB rest frame for the GRBs with known redshift. The first column is the GRB name. The T_{90} and T_{50} durations in the GRB rest frame are in the second and the third columns. The last column contains the comments.

Table 9 lists redshift measurements of *Swift* GRBs and their associated references.

4.1. Short GRBs with Extended Emission

A distinct class of short-duration GRBs (S-GRBs) has been claimed based on their prompt emission properties, called S-GRB with extended emission (E.E.; e.g., Norris et al. 2000; Barthelmy et al. 2005b). The initial short spike of an S-GRB with E.E. shows negligible spectral lag which is one of the strong indications that the burst is an S-GRB (Norris et al. 2000). Ten GRBs in our catalog have been classified as S-GRBs with E.E. by Norris et al. (2010) and these are labeled as such throughout this paper.¹⁶ The BAT light curves of 10 S-GRBs with E.E. included in this catalog are shown in Figure 3. The initial short spike is usually composed of multiple pulses with a total duration of less than 2 s. The E.E. lasts from a few tens to a few hundreds of seconds. We distinguish among long GRBs (L-GRBs), S-GRBs, and an S-GRBs with an E.E. throughout the paper to investigate the prompt emission properties of these three different classes of GRBs. Table 10 summarizes the statistics of the samples in the catalog based on the classifications. The fractions of L-GRBs, S-GRBs, and S-GRBs with E.E. in

¹⁶ GRB 060614 is classified as an L-GRB because the duration of the initial spike is ~ 6 s long. GRB 050911 is also classified as an L-GRB because our standard pipeline process does not detect the significant extended emission as reported in Norris et al. (2010). The T_{90} of GRB 050911 based on our analysis is 16.2 s.

Table 6
BAT Time-averaged Spectral Parameters

| GRB | α^{PL} | $K_{50}^{\text{PL}}(\text{a})$ | χ_{PL}^2 | α^{CPL} | $E_{\text{peak}}^{\text{obs}}$ (keV) | $K_{50}^{\text{CPL}}(\text{b})$ | χ_{CPL}^2 | Note |
|---------|----------------------------|--------------------------------|----------------------|----------------------------|---|---------------------------------|-----------------------|------|
| 041217 | $-1.452^{+0.064}_{-0.064}$ | $417.0^{+15.4}_{-15.4}$ | 73.2 | $-0.663^{+0.309}_{-0.29}$ | $91.5^{+22.8}_{-12.0}$ | $97.5^{+37.3}_{-25.7}$ | 49.2 | |
| 041219A | ... | ... | ... | ... | ... | ... | ... | (1) |
| 041219B | ... | ... | ... | ... | ... | ... | ... | (1) |
| 041219C | $-2.007^{+0.087}_{-0.089}$ | $103.0^{+5.4}_{-5.4}$ | 44.6 | ... | ... | ... | ... | |
| 041220 | $-1.672^{+0.120}_{-0.122}$ | $56.2^{+3.9}_{-4.0}$ | 30.5 | ... | ... | ... | ... | |
| 041223 | $-1.153^{+0.030}_{-0.03}$ | $106.0^{+1.8}_{-1.8}$ | 33.4 | ... | ... | ... | ... | |
| 041224 | $-1.731^{+0.058}_{-0.058}$ | $43.2^{+1.4}_{-1.4}$ | 62.8 | $-0.984^{+0.281}_{-0.264}$ | $68.9^{+11.7}_{-7.0}$ | $10.1^{+3.7}_{-2.6}$ | 36.9 | |
| 041226 | $-1.416^{+0.430}_{-0.417}$ | $3.4^{+0.8}_{-0.8}$ | 85.1 | ... | ... | ... | ... | |
| 041228 | $-1.617^{+0.077}_{-0.077}$ | $55.1^{+2.3}_{-2.3}$ | 64.6 | ... | ... | ... | ... | |
| 050117 | $-1.519^{+0.042}_{-0.042}$ | $44.5^{+0.9}_{-0.9}$ | 44.4 | $-1.171^{+0.182}_{-0.172}$ | $130.3^{+70.6}_{-26.7}$ | $6.4^{+1.3}_{-1.0}$ | 32.2 | |

Notes.^a In units of 10^{-4} photons $\text{cm}^{-2} \text{ s}^{-1} \text{ keV}^{-1}$.^b In units of 10^{-3} photons $\text{cm}^{-2} \text{ s}^{-1} \text{ keV}^{-1}$.¹ The event data are not available.² The event data of the part of the burst emission are not available.³ No error because of reduced chi2 > 2.⁴ $K_{50}^{\text{PL}} = 2.9^{+0.5}_{-0.6}$ for the spectrum based on the event data and $K_{50}^{\text{PL}} = 28.1^{+0.4}_{-0.4}$ for the spectrum based on the DPH data.⁵ $K_{50}^{\text{PL}} = 4.4^{+0.4}_{-0.4}$ for the spectrum based on the event data and $K_{50}^{\text{PL}} = 3.4^{+0.2}_{-0.2}$ for the spectrum based on the DPH data.⁶ K_{50}^{CPL} is an upper limit.

(This table is available in its entirety in a machine-readable form in the online journal. A portion is shown here for guidance regarding its form and content.)

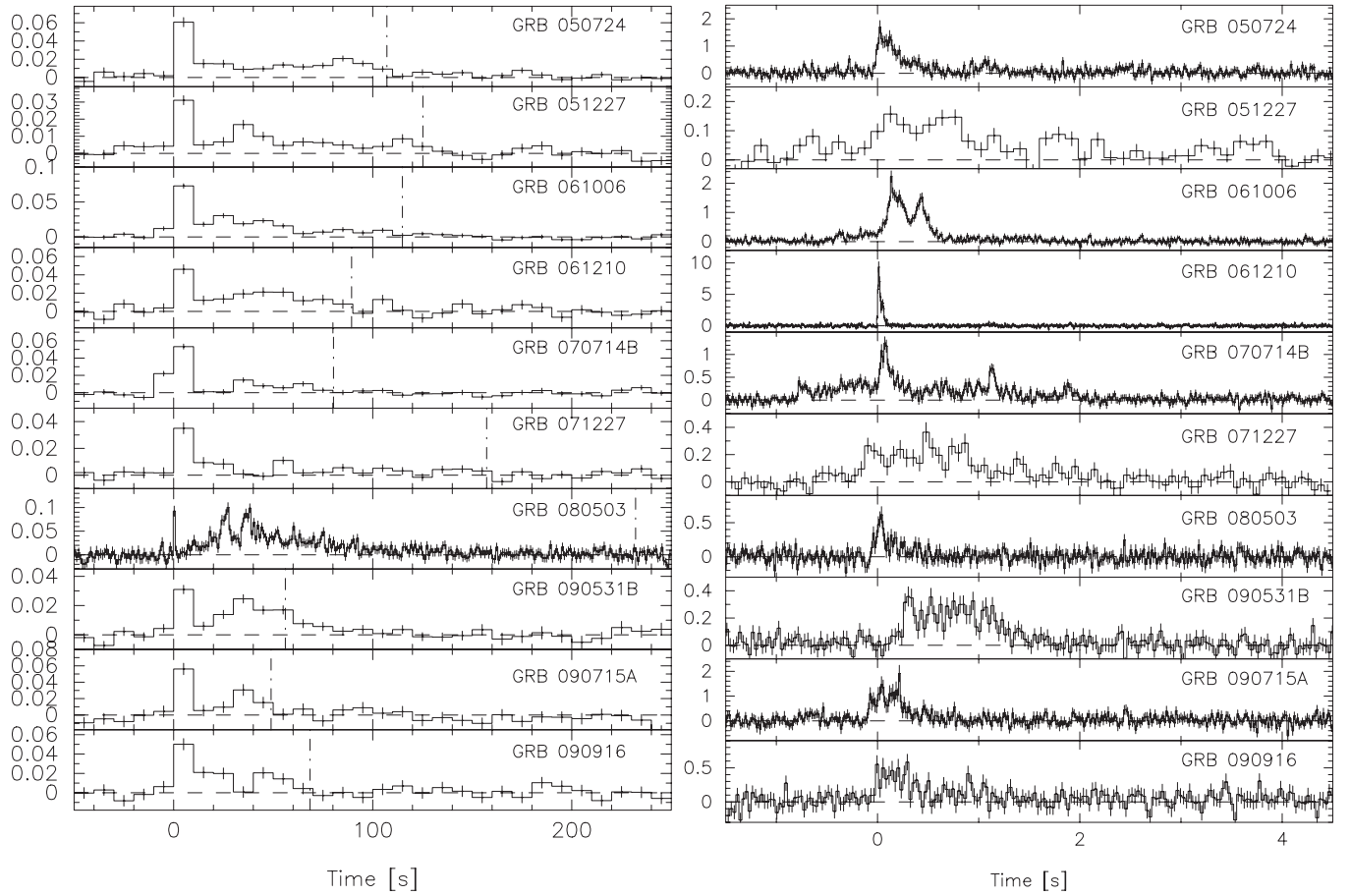


Figure 3. BAT mask-weighted light curves in the 15–150 keV band in a coarse binning (left) and a fine binning (right) for short GRBs with extended emission. The vertical dash-dotted lines in the coarse binning light curves show the emission end time found by `battblocks`.

Table 7
BAT Time-resolved Spectral Parameters

| GRB | Start (s) | Stop (s) | α^{PL} | $K_{50}^{\text{PL}}(\text{a})$ | χ^2 | $F_{\text{PL}}(15-150)(\text{b})$ | α^{CPL} | $E_{\text{peak}}^{\text{obs}}$ (keV) | $K_{50}^{\text{CPL}}(\text{c})$ | χ^2 | $F_{\text{CPL}}(15-150)(\text{b})$ | Note |
|---------|-----------|----------|----------------------------|--------------------------------|----------|-----------------------------------|----------------------------|--------------------------------------|---------------------------------|----------|------------------------------------|------|
| 041217 | 0.824 | 5.812 | $-1.385^{+0.064}_{-0.064}$ | $499.0^{+18.8}_{-18.8}$ | 78.2 | 48.4 ± 1.9 | $-0.517^{+0.319}_{-0.297}$ | $93.6^{+21.1}_{-11.8}$ | $126.0^{+49.2}_{-33.3}$ | 50.2 | 46.3 ± 2.1 | |
| 041217 | 5.812 | 7.888 | $-1.763^{+0.191}_{-0.198}$ | $210.0^{+25.5}_{-25.9}$ | 54.5 | 19.3 ± 2.5 | ... | ... | ... | ... | ... | |
| 041219C | 0.000 | 6.000 | $-1.912^{+0.094}_{-0.096}$ | $139.0^{+7.8}_{-7.8}$ | 52.7 | 12.7 ± 0.7 | ... | ... | ... | ... | ... | |
| 041219C | 6.000 | 9.000 | $-2.168^{+0.169}_{-0.179}$ | $88.8^{+10.4}_{-10.7}$ | 54.4 | 8.3 ± 0.9 | ... | ... | ... | ... | ... | |
| 041219C | 9.000 | 12.000 | $-2.060^{+0.300}_{-0.332}$ | $45.1^{+9.5}_{-9.9}$ | 42.3 | 4.2 ± 0.8 | ... | ... | ... | ... | ... | |
| 041220 | -0.208 | 1.728 | $-1.479^{+0.116}_{-0.117}$ | $126.0^{+8.3}_{-8.3}$ | 52.0 | 12.0 ± 0.9 | ... | ... | ... | ... | ... | |
| 041220 | 1.728 | 2.936 | $-1.862^{+0.236}_{-0.25}$ | $59.1^{+9.4}_{-9.7}$ | 53.9 | 5.4 ± 0.9 | ... | ... | ... | ... | ... | |
| 041220 | 2.936 | 6.812 | $-2.029^{+0.360}_{-0.408}$ | $19.3^{+5.0}_{-5.3}$ | 40.1 | 1.8 ± 0.4 | ... | ... | ... | ... | ... | |
| 041223 | -10.536 | -0.544 | $-1.363^{+0.388}_{-0.381}$ | $17.1^{+4.0}_{-4.0}$ | 61.5 | 1.7 ± 0.4 | ... | ... | ... | ... | ... | |
| 041223 | -0.544 | -0.124 | $-1.529^{+0.400}_{-0.408}$ | $88.9^{+21.9}_{-22.3}$ | 48.5 | 8.4 ± 2.3 | ... | ... | ... | ... | ... | |

Notes.

^a In units of 10^{-4} photons $\text{cm}^{-2} \text{s}^{-1} \text{keV}^{-1}$.

^b In units of 10^{-8} erg $\text{cm}^{-2} \text{s}^{-1}$.

^c In units of 10^{-3} photons $\text{cm}^{-2} \text{s}^{-1} \text{keV}^{-1}$.

¹ Not enough statistics to perform the spectral fit.

² No error because reduced chi2 is greater than 2.

³ K_{50}^{CPL} is an upper limit.

⁴ $F_{\text{PL}}(15-150)$ is an upper limit.

⁵ Bad quality of the spectrum.

⁶ Spectral parameters are not constrained by a CPL fit.

(This table is available in its entirety in a machine-readable form in the online journal. A portion is shown here for guidance regarding its form and content.)

Table 8
BAT GRB T_{90} and T_{50} Durations in the 140–220 keV Band
at the GRB Rest Frame

| GRB | T_{90}^{SFC} (s) | T_{50}^{SFC} (s) | Note |
|---------|------------------------------|------------------------------|------|
| 050126 | 8.73 | 4.80 | |
| 050223 | ... | ... | (1) |
| 050315 | 13.99 | 6.93 | |
| 050318 | 5.68 | 3.02 | |
| 050319 | 33.29 | 28.15 | |
| 050401 | 8.37 | 6.53 | |
| 050416A | ... | ... | (1) |
| 050505 | 11.37 | 4.55 | |
| 050509B | ... | ... | (1) |
| 050525A | 4.24 | 2.89 | |

Notes.

¹ Battblocks failed because of the weak signal in the light curve.

² The event data of the part of the burst emission are not available.

(This table is available in its entirety in a machine-readable form in the online journal. A portion is shown here for guidance regarding its form and content.)

Table 9
Redshifts of *Swift* GRBs

| GRB | Redshift | Reference |
|---------|----------|-----------|
| 050126 | 1.290 | (2) |
| 050223 | 0.584 | (3) |
| 050315 | 1.950 | (4) |
| 050318 | 1.444 | (4) |
| 050319 | 3.2425 | (1) |
| 050401 | 2.8983 | (1) |
| 050416A | 0.6528 | (5) |
| 050505 | 4.275 | (6) |
| 050509B | 0.226 | (7) |
| 050525A | 0.606 | (8) |

Notes.

¹ Fynbo et al. (2009).

² Berger et al. (2005a).

³ Pellizza et al. (2006).

⁴ Berger et al. (2005b).

⁵ Soderberg et al. (2007).

⁶ Berger et al. (2006).

⁷ Gehrels et al. (2005).

⁸ Della Valle et al. (2006).

⁹ Berger & Becker (2005).

¹⁰ Berger et al. (2005c).

¹¹ Jakobsson et al. (2006).

¹² Mirabal et al. (2007).

¹³ Kawai et al. (2006).

(This table is available in its entirety in a machine-readable form in the online journal. A portion is shown here for guidance regarding its form and content.)

the catalog are 89%, 8%, and 2%, respectively. The spectral parameters and the energy fluences of the initial short spike are reported in Tables 11 and 12. Note that our definition of S-GRBs is whether T_{90} is smaller than 2 s or not. The GRBs classified as S-GRBs or S-GRBs with E.E. in our study are also identified in Table 1.

4.2. BAT GRB Position and Sky Locations

Figure 4 shows the angular difference between the BAT ground position and the enhanced XRT position (Evans et al.

Table 10
Statistics of the BAT2 GRB Catalog

| Class | Number of GRBs | Fraction | Classification |
|--------------|----------------|----------|----------------------|
| L-GRB | 424 | 89% | $T_{90} \geq 2$ s |
| S-GRB | 38 | 8% | $T_{90} < 2$ s |
| S-GRB w/E.E. | 10 | 2% | Norris et al. (2010) |
| Unknown | 4 | 1% | Incomplete/lost data |

Table 11
Spectral Parameters of the Initial Short Spikes of the Short GRBs with E.E.

| GRB | Start (s) | Stop (s) | α^{PL} | $K_{50}^{\text{PL(a)}}$ | χ^2 |
|---------|--------------|-------------|-------------------------|----------------------------|----------|
| 050724 | -0.024 | 0.416 | $-1.50^{+0.14}_{-0.14}$ | $515.2^{+40.9}_{-41.1}$ | 50.9 |
| 051227 | -0.848 | 0.828 | $-0.94^{+0.23}_{-0.25}$ | $61.0^{+7.9}_{-8.0}$ | 65.6 |
| 061006 | -23.24 | -22.20 | $-0.86^{+0.07}_{-0.07}$ | $445.3^{+17.7}_{-17.8}$ | 50.8 |
| 061210 | -0.004 | 0.080 | $-0.69^{+0.12}_{-0.12}$ | $2755.1^{+209.0}_{-209.8}$ | 58.2 |
| 070714B | -1 | -2 | $-0.98^{+0.08}_{-0.08}$ | $158.2^{+7.2}_{-7.2}$ | 43.0 |
| 071227 | -0.144 | 1.872 | $-0.90^{+0.22}_{-0.24}$ | $98.6^{+12.1}_{-12.3}$ | 51.0 |
| 080503 | -0.048 | 0.436 | $-1.62^{+0.23}_{-0.23}$ | $130.6^{+19.3}_{-19.6}$ | 66.0 |
| 090531B | 0.252 | 1.300 | $-0.99^{+0.16}_{-0.16}$ | $148.4^{+12.0}_{-12.1}$ | 63.3 |
| 090715A | -0.12 | 0.84 | $-0.99^{+0.19}_{-0.20}$ | $348.9^{+38.3}_{-38.8}$ | 55.0 |
| 090916 | 0.0 | 0.35 | $-1.38^{+0.30}_{-0.30}$ | $236.5^{+44.5}_{-44.5}$ | 72.6 |

Note. ^a In units of 10^{-4} photons $\text{cm}^{-2} \text{s}^{-1} \text{keV}^{-1}$.

2009). The BAT ground position is within 1/1, 1/8, and 3/5 from the XRT position for 68%, 90%, and 99% of the bursts, respectively. Figure 5 shows the sky map of the 476 BAT GRBs in galactic coordinates. L-GRBs, S-GRBs, and S-GRBs with E.E. are marked in different colors.

4.3. Durations and Hardness

The histograms of T_{90} and T_{50} in the BAT full energy band are shown in Figure 6. The average of the BAT T_{90} and T_{50} durations are 71 and 31 s, respectively. In Figure 7, we compare the T_{90} distributions of BAT, the Burst and Transient Source Experiment (BATSE), *BeppoSAX*, and the *High Energy Transient Explorer 2* satellite (*HETE-2*). The BATSE T_{90} are extracted from the 4B catalog (Paciesas et al. 1999), and they are measured in the 50–300 keV band. The *BeppoSAX* T_{90} are extracted from Frontera et al. (2009), and they are measured using the light curve of the GRBM instrument in the 40–700 keV band. The *HETE-2* T_{90} are extracted from Pélangeon et al. (2008), and they are measured using the light curve of the FREGATE instrument in the 6–80 keV band. There is a clear shift in the peak of the L-GRB populations measured with different instruments. The peak of L-GRBs T_{90} distribution from the BATSE, the *BeppoSAX*, and the *HETE-2* samples is around 10–30 s, whereas the BAT distribution is around 70 s. It is clear from this comparison that the duration measurement depends upon the sensitivity of the instruments. Another distinct difference in the BATSE distribution compared to that of the BAT, the *BeppoSAX*, and the *HETE-2* distributions is a clear bimodality between S-GRBs and L-GRBs (e.g., Kouveliotou et al. 1993). The lack of S-GRBs in imaging instruments such as the BAT and *HETE-2* is a result of the larger number of photons needed to “image” a GRB with these instruments. This requirement is usually difficult to achieve for S-GRBs because they are usually faint and their emissions are short. However, note that BAT has been triggering and localizing S-GRBs at a much higher rate than other

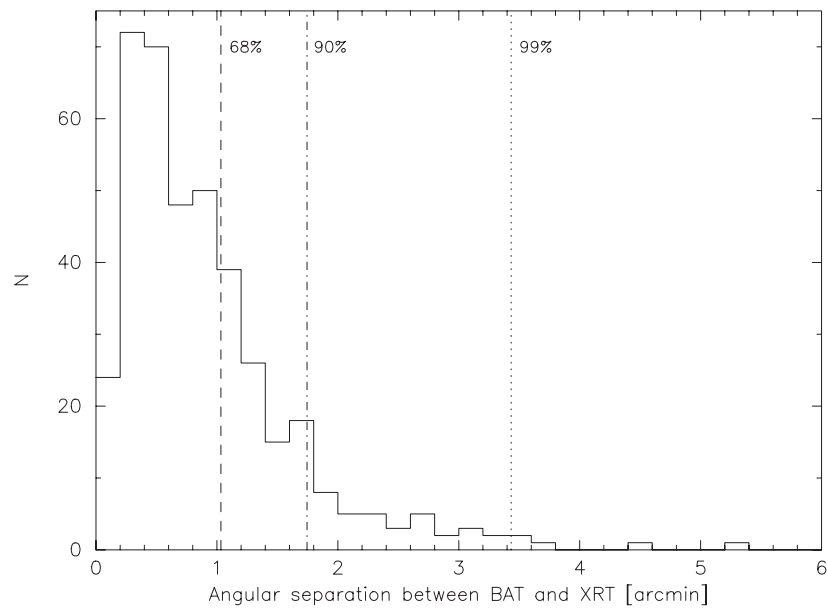


Figure 4. Histogram of the angular difference between the BAT ground position and the XRT position.

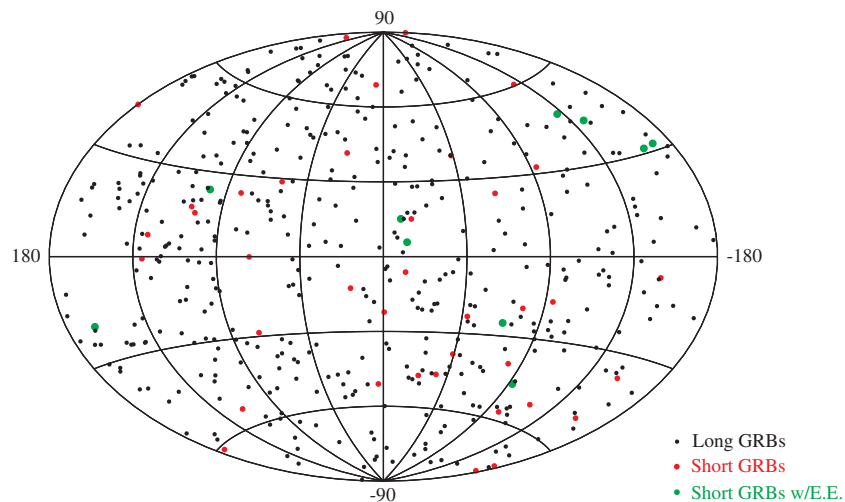


Figure 5. Sky distribution of the 476 BAT bursts in Galactic coordinates with long GRBs in black, short GRBs in red, and short GRBs with extended emissions in green.

(A color version of this figure is available in the online journal.)

Table 12
BAT GRB Energy Fluence of the Initial Short Spikes of the Short GRB with E.E.

| GRB Name | Spectral Model | S (15–25) | S (25–50) | S (50–100) (10^{-8} erg cm^{-2}) | S (100–150) | S (15–150) |
|----------|----------------|---------------|---------------|--|----------------|----------------|
| 050724 | PL | 2.9 ± 0.4 | 5.3 ± 0.4 | 7.5 ± 0.8 | 5.7 ± 0.9 | 21.5 ± 1.9 |
| 051227 | PL | 0.8 ± 0.2 | 2.0 ± 0.3 | 4.2 ± 0.6 | 4.3 ± 1.0 | 11.3 ± 1.6 |
| 061006 | PL | 3.3 ± 0.3 | 8.9 ± 0.4 | 19.6 ± 0.8 | 21.0 ± 1.4 | 52.7 ± 2.3 |
| 061210 | PL | 1.4 ± 0.2 | 4.2 ± 0.4 | 10.5 ± 0.8 | 12.4 ± 1.5 | 28.4 ± 2.4 |
| 070714B | PL | 3.7 ± 0.4 | 9.4 ± 0.5 | 19.2 ± 1.0 | 19.5 ± 1.6 | 51.8 ± 2.6 |
| 071227 | PL | 1.4 ± 0.4 | 3.9 ± 0.6 | 8.3 ± 1.1 | 8.8 ± 1.8 | 22.4 ± 2.9 |
| 080503 | PL | 0.9 ± 0.2 | 1.5 ± 0.2 | 2.0 ± 0.4 | 1.5 ± 0.4 | 5.9 ± 0.9 |
| 090531B | PL | 1.2 ± 0.2 | 3.1 ± 0.3 | 6.3 ± 0.6 | 6.3 ± 1.0 | 16.8 ± 1.6 |
| 090715A | PL | 2.7 ± 0.6 | 6.7 ± 0.9 | 13.4 ± 1.5 | 13.5 ± 2.4 | 36.3 ± 4.0 |
| 090916 | PL | 0.9 ± 0.3 | 1.9 ± 0.4 | 2.9 ± 0.6 | 2.3 ± 0.8 | 8.0 ± 1.6 |

GRB imaging instruments because of its large effective area and its sophisticated flight software. As mentioned in Frontera et al. (2009), the lack of S-GRBs in the *BeppoSAX* samples is likely to be due to the lower efficiency of the trigger system to S-GRBs.

Figure 8 shows the fluence ratio between the 50–100 keV and the 25–50 keV band versus the T_{90} and T_{50} durations of the BAT GRBs. It is clear from the figures that there is not a large number of S-GRBs that have soft spectra. Most of the S-GRBs have a

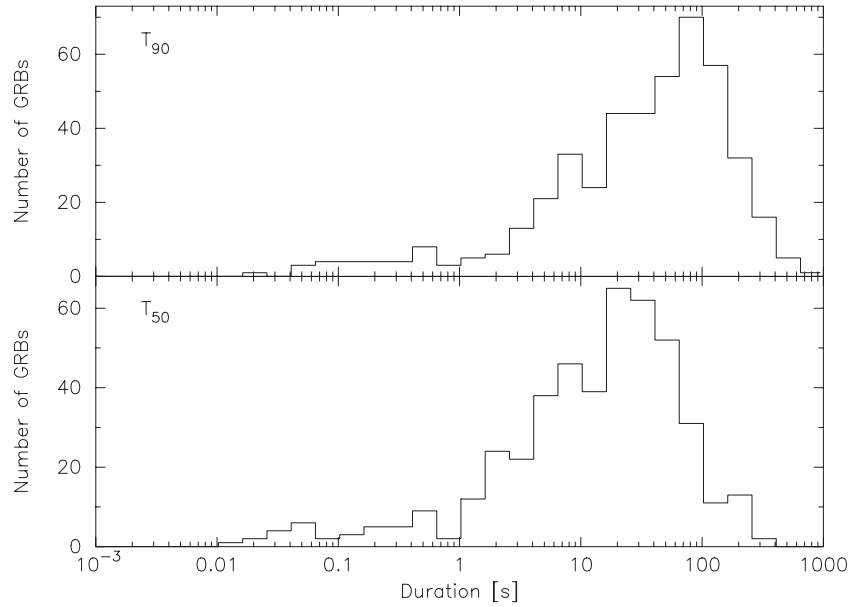


Figure 6. T_{90} (top) and T_{50} (bottom) distributions from the BAT mask-weighted light curves in the 15–350 keV band.

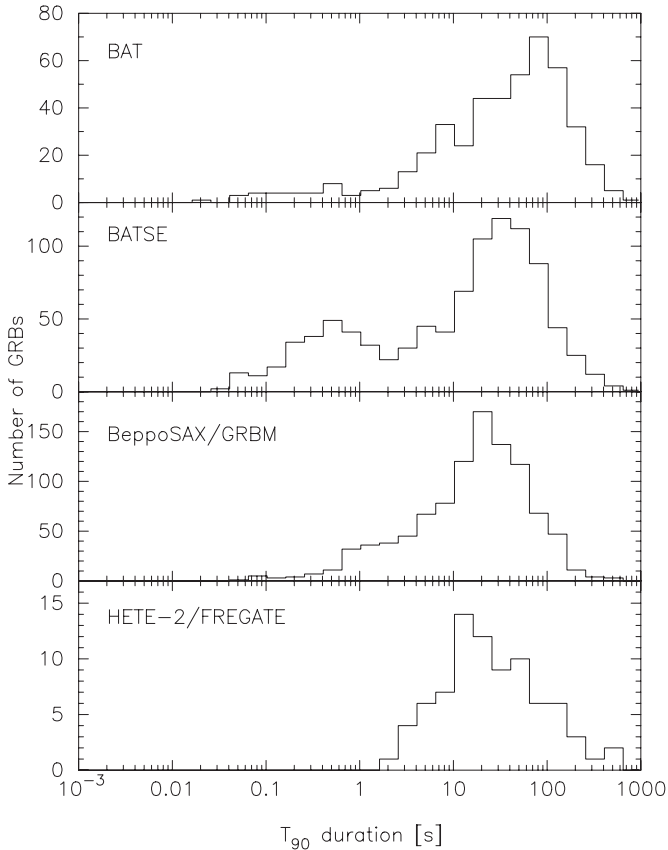


Figure 7. From top to bottom, T_{90} distribution of BAT from the mask-weighted light curves in the 15–350 keV band, BATSE from the light curves in the 50–350 keV band, *BeppoSAX* from the light curves of the GRBM instrument in the 40–700 keV band, and *HETE-2* from the light curves of the FREGATE instrument in the 6–80 keV band.

fluence ratio of about 2. On the other hand, the averaged fluence ratio of the L-GRBs is 1.3. The Kolmogorov–Smirnov (K-S) test probability of the fluence ratio between L-GRBs and S-GRBs is 8.3×10^{-20} . Based on this comparison, we can conclude that the S-GRBs are generally harder than the L-GRBs. However,

note that there is a large overlap in hardness between L-GRBs and S-GRBs in the BAT sample. The S-GRBs with E.E. overlap the L-GRB samples.

The comparisons in the fluence ratio– T_{90} plane for the BAT, the BATSE, the *BeppoSAX*, and the *HETE-2* GRBs are shown in Figure 9. Both fluences and T_{90} values for the BATSE sample are extracted from the 4B catalog. For the *BeppoSAX* sample, we used the best-fit simple PL model in the catalog (Frontera et al. 2009) to calculate the fluence ratios in the 50–100 keV and the 25–50 keV band. For the *HETE-2* sample, we calculated the fluences in those energy bands using the spectral parameters reported in Sakamoto et al. (2005) and Pélangéon et al. (2008). We only calculated the fluences for sources listed with CPL or Band parameters.¹⁷ The T_{90} values of the *HETE-2* sample are from Pélangéon et al. (2008). As seen in Figure 9, the GRB samples of different missions are overlaid on each other.

4.4. Peak Fluxes and Fluences

Figure 10 shows the 1 s and the 20 ms peak photon fluxes versus the fluence in the 15–150 keV band. As we showed in the BAT1 catalog, there is a positive correlation between peak photon flux and fluence. Based on the correlation between the 20 ms peak flux and the 15–150 keV fluence (lower panel of Figure 10), it is now clear that most of the BAT S-GRBs populate a low fluence but high peak flux region. For S-GRBs, the 1 s peak flux is systematically lower than the 20 ms peak flux because the 1 s time window is usually predominantly larger than the actual S-GRB duration used for calculating the flux. That the S-GRB population has low fluence and high peak flux in the BAT sample could be due to the selection effect of the imaging requirement in the trigger algorithm (e.g., more detected photons are needed to image the source).

The fluence in the 50–150 keV band versus that in the 15–50 keV band for the BAT GRBs is shown in the top panel of Figure 11. In this figure we also indicate the distribution expected for a Band function with a low-energy photon index

¹⁷ Because of this spectral model requirement, we are excluding a large number of X-ray flashes in the *HETE-2* sample where a PL is the usual accepted model.

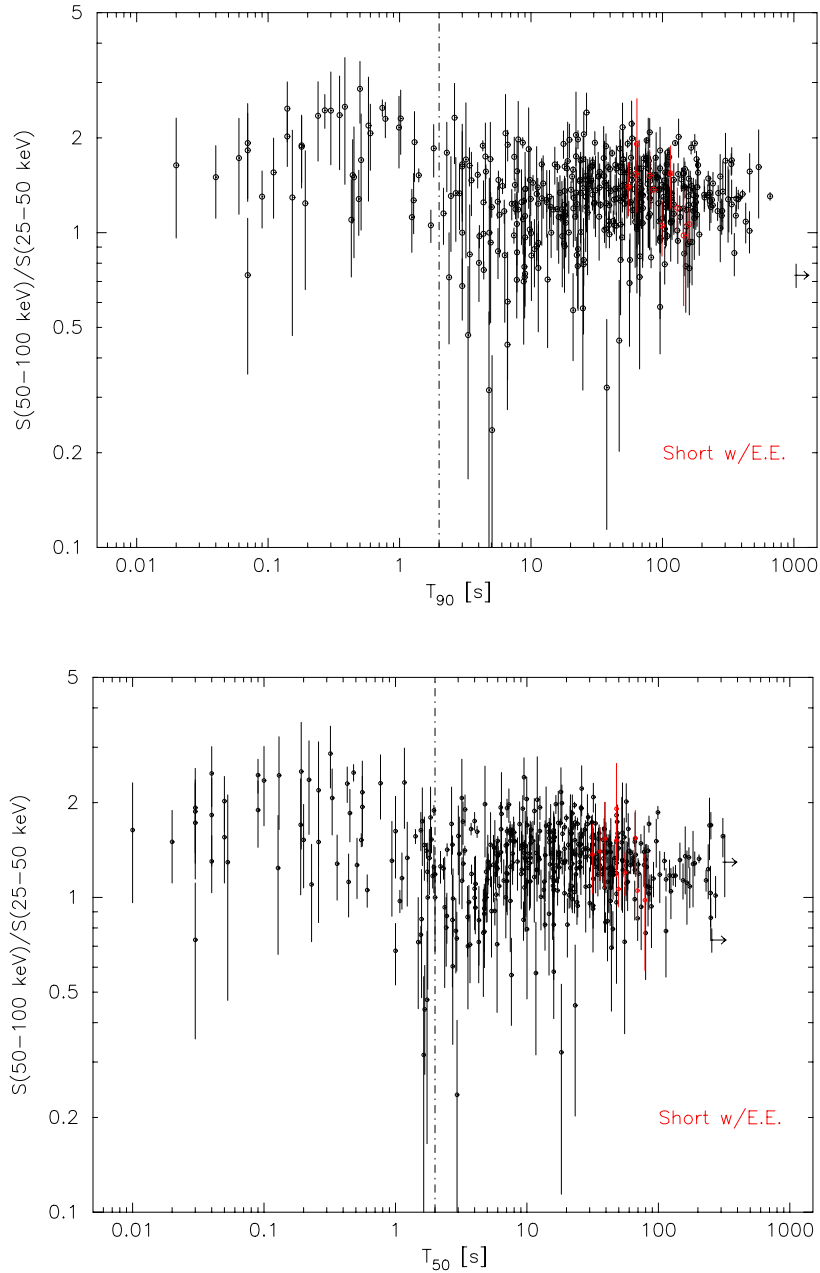


Figure 8. Fluence ratio between the 50–100 keV and the 25–50 keV bands plotted with respect to T_{90} (top) and T_{50} (bottom). Short GRBs with an E.E. are shown in red. The dash-dotted vertical line shows $T_{90} = 2$ s.

(A color version of this figure is available in the online journal.)

of -1 and a high-energy photon of -2.5 . Comparing to these lines, we see that 43% of the BAT GRBs have $E_{\text{peak}}^{\text{obs}} > 100$ keV, 50% of the BAT GRBs have $30 \text{ keV} < E_{\text{peak}}^{\text{obs}} \leq 100$ keV, and 7% of the BAT GRBs have $E_{\text{peak}}^{\text{obs}} \leq 30$ keV. The S-GRBs generally have low fluences with hard spectra and a small overlap with the L-GRB properties. On the other hand, the S-GRBs with E.E. lie in the same region as the L-GRBs. However, the initial short spikes of the S-GRBs with E.E. have similar characteristics to the S-GRBs. The bottom panel of Figure 11 compares the BAT, the BATSE, and the *HETE-2* GRBs in the same fluence–fluence plane. The fluences for the BATSE sample and the *HETE-2* are calculated using the best-fit spectral parameters of a CPL model and a Band function as reported in Kaneko et al. (2006) and Pélagion et al. (2008). The majority of the BATSE bursts

have high fluences with hard spectra. The *HETE-2* and the BAT samples have a similar characteristic in the fluences. The similar number of GRBs in the range $E_{\text{peak}}^{\text{obs}} > 100$ keV and $30 \text{ keV} < E_{\text{peak}}^{\text{obs}} \leq 100$ keV is consistent with the *HETE-2* GRB sample (Sakamoto et al. 2005). The systematically smaller number of GRBs with a soft spectrum ($E_{\text{peak}}^{\text{obs}} \leq 30$ keV) in the BAT is likely due to a lack of sensitivity below 15 keV for the BAT. Differences in BAT, *HETE-2*, and BATSE are very likely due to the different response and trigger energy as shown in Figure 12.

4.5. Time-averaged Spectral Parameters

Figure 13 shows the histograms of the BAT time-averaged photon index from a PL fit for L-GRBs, S-GRBs, S-GRBs with E.E. and the initial short spikes of the S-GRBs with E.E. A

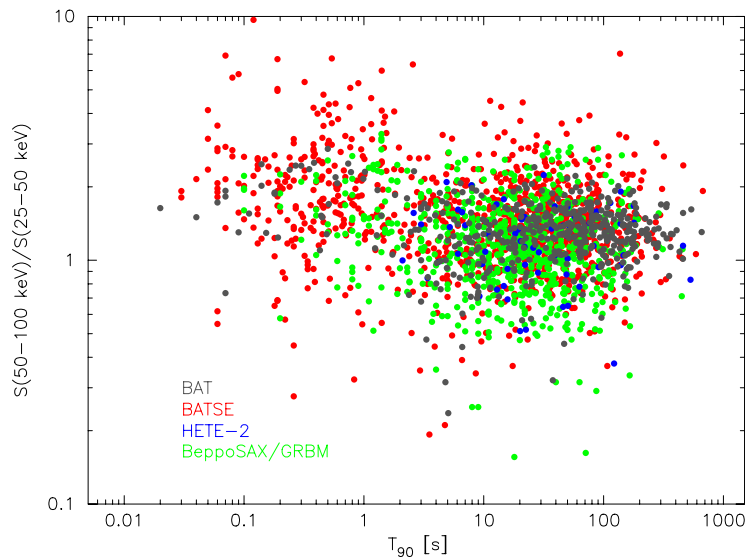


Figure 9. Fluence ratio between the 50–100 keV and the 25–50 keV bands vs. T_{90} for BAT (dark gray), BATSE (red), *HETE-2* (blue), and *BeppoSAX* (green) GRBs. (A color version of this figure is available in the online journal.)

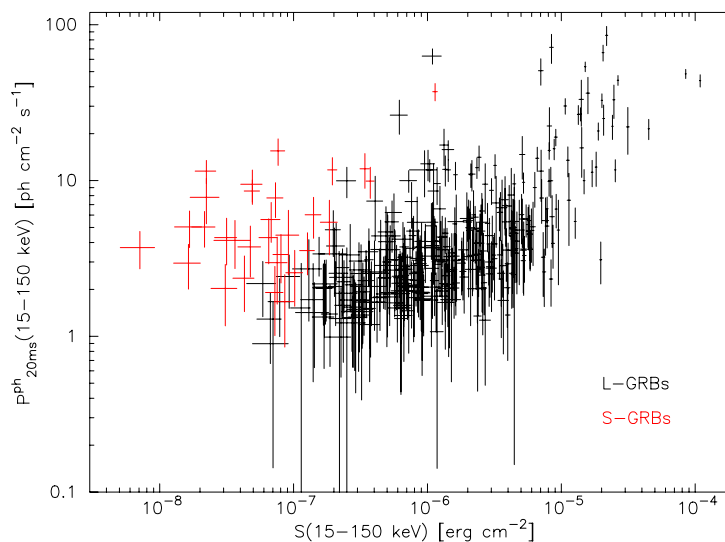
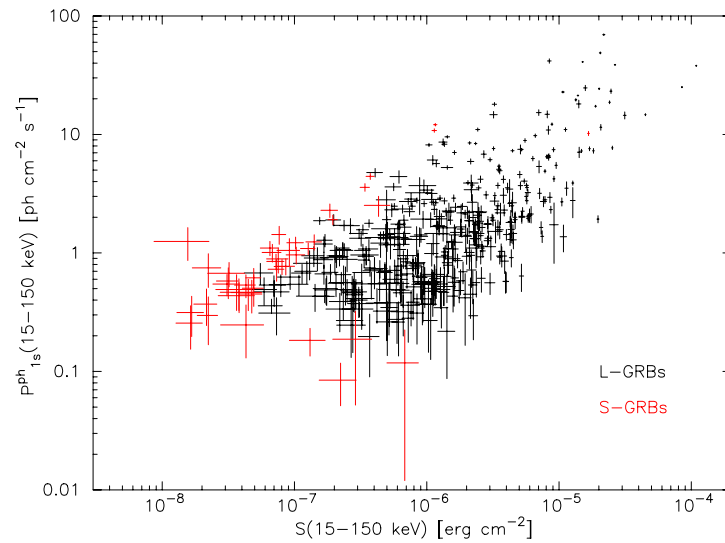


Figure 10. Distributions of 1 s peak photon flux (top) and 20 ms peak photon flux (bottom) in the 15–150 keV band plotted vs. energy fluence in the 15–150 keV band.

(A color version of this figure is available in the online journal.)

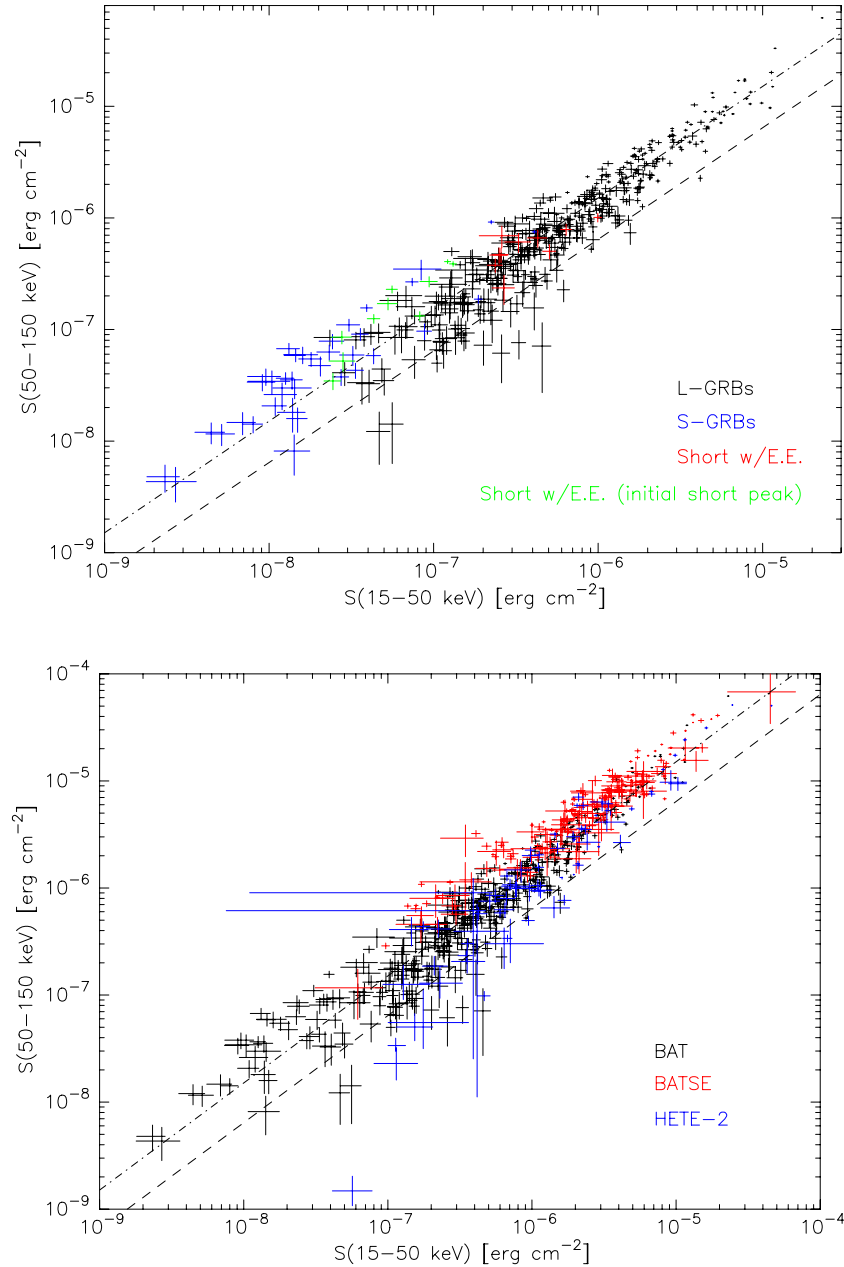


Figure 11. Top: distribution of the energy fluence in the 50–150 keV band vs. that in the 15–50 keV band for the BAT GRBs. L-GRBs are in black, S-GRBs are in blue, S-GRBs with E.E. are in red, and the initial short spikes of S-GRBs with E.E. are in green. The dash-dotted line is the distribution expected for the case of the Band function with $\alpha = -1$, $\beta = -2.5$, and $E_{\text{peak}}^{\text{obs}} = 100$ keV. The dashed line is for the case of the Band function with $\alpha = -1$, $\beta = -2.5$, and $E_{\text{peak}}^{\text{obs}} = 30$ keV. Bottom: distribution in the same plane as top among different missions. The BAT sample is in black, the BATSE sample is in red, and the HETE-2 sample is in blue. The definitions of the dash-dotted and dashed lines are same as in the top panel.

(A color version of this figure is available in the online journal.)

Gaussian fit to the histogram of PL photon indices of L-GRBs shows a peak at -1.6 with a σ of 0.3 . This BAT photon index based on a PL fit is systematically steeper than the typical low-energy photon index α (~ -1) and also shallower than the high-energy photon index β (~ -2.5) based on a Band function fit (e.g., Kaneko et al. 2006). As demonstrated in the detailed spectral simulation study of Sakamoto et al. (2009), the distribution of the BAT photon index in a PL fit reflects the fact that more than half of $E_{\text{peak}}^{\text{obs}}$ in BAT GRBs are located within the BAT energy range (15–150 keV). This is consistent with the discussion in Section 4.4 that 50% of $E_{\text{peak}}^{\text{obs}}$ in the BAT GRBs are located $30 \text{ keV} < E_{\text{peak}}^{\text{obs}} \leq 100 \text{ keV}$ assuming typical spectral

parameters from a fit to a Band function. The histogram of PL photon indices of S-GRBs has a shift toward a shallower index compared to that of the L-GRBs. The time-averaged PL photon index for the S-GRBs is -1.2 . We used a K-S test to check whether the L-GRBs and the S-GRBs are drawn from the same population. The K-S test statistic of 10^{-7} strongly indicates that the time-averaged PL photon index distributions of the L-GRBs and S-GRBs are different. We confirm in the BAT GRB sample that S-GRBs in general have a harder spectrum than that of L-GRBs (e.g., Kouveliotou et al. 1993; Ghirlanda et al. 2009). Although the number in the former sample is limited, the time-averaged PL photon index of S-GRBs with E.E. is consistent

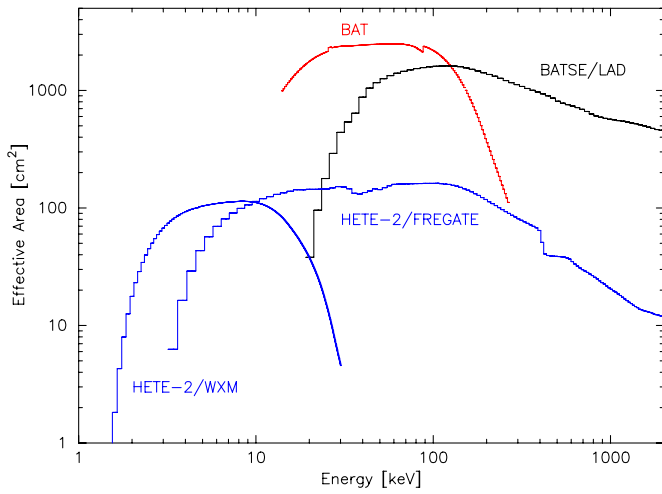


Figure 12. Comparison of the effective area (on-axis) of BATSE/LAD (from the BATSE energy response file of trigger no. 1123 at the CGRO/BATSE Gamma-Ray Burst Catalog: <http://heasarc.gsfc.nasa.gov/W3Browse/cgro/batsegrb.html>), *Swift*/BAT and *HETE*-2 (WXM, Shirasaki et al. 2003; FREGATE, Atteia et al. 2003).

(A color version of this figure is available in the online journal.)

with the L-GRBs. On the other hand, the PL photon index of the initial short spikes of the S-GRBs with E.E. is much more consistent with that of the S-GRBs.

Figure 14 shows the BAT time-averaged photon index from a PL fit versus the fluence in the 15–150 keV band. Similar to the trend in Figures 11 and 13, the S-GRBs are located in a lower fluence and a harder spectral region compared to the L-GRBs. The time-averaged properties of the S-GRBs with E.E. overlap with the L-GRBs in the PL photon index–fluence plane. The initial short spikes of the S-GRBs with E.E. seem consistent with the properties of S-GRBs in this plane, but lie in a systematically higher fluence region than the S-GRBs.

The low-energy photon index α and $E_{\text{peak}}^{\text{obs}}$ from a CPL fit are shown for the BAT, the BATSE, and the *HETE*-2 GRBs in Figure 15. Seventy-seven out of 456 time-averaged spectra (17%) in the BAT sample show a significant improvement of χ^2 in a CPL fit over a PL fit ($\Delta\chi^2 > 6$). The BATSE and the *HETE*-2 spectral parameters from a CPL fit are taken from Kaneko et al. (2006) and Pélangéon et al. (2008), respectively. The low-energy photon index α is consistent among all the instruments. However, most of the $E_{\text{peak}}^{\text{obs}}$ of the BATSE GRBs are larger than 100 keV, whereas the majority of $E_{\text{peak}}^{\text{obs}}$ in the BAT and the *HETE*-2 GRBs are less than 100 keV. This is more clearly represented in the histograms of $E_{\text{peak}}^{\text{obs}}$ shown in Figure 16. The Gaussian fits to the log-normal $E_{\text{peak}}^{\text{obs}}$ histograms of the BAT, the BATSE, and the *HETE*-2 samples reveal the peaks to be at 79 keV, 320 keV, and 65 keV with σ in $\log(E_{\text{peak}}^{\text{obs}})$ of 0.18, 0.22, and 0.31, respectively. The K-S test probabilities in the log-normal $E_{\text{peak}}^{\text{obs}}$ distributions for the BAT and the BATSE bursts, and the BAT and the *HETE*-2 bursts are 9×10^{-21} and 0.15, respectively. As clearly seen in these histograms, although the peaks and the widths of the $E_{\text{peak}}^{\text{obs}}$ distributions differ among the instruments, they are overlapping. Moreover, there is no sign of a bimodal $E_{\text{peak}}^{\text{obs}}$ distribution in the measurements from a single instrument. Therefore, we may conclude that “true” $E_{\text{peak}}^{\text{obs}}$ has a single broad log-normal distribution. The difference of the $E_{\text{peak}}^{\text{obs}}$ distributions among the GRB instruments is very likely due to an instrumental selection effect.

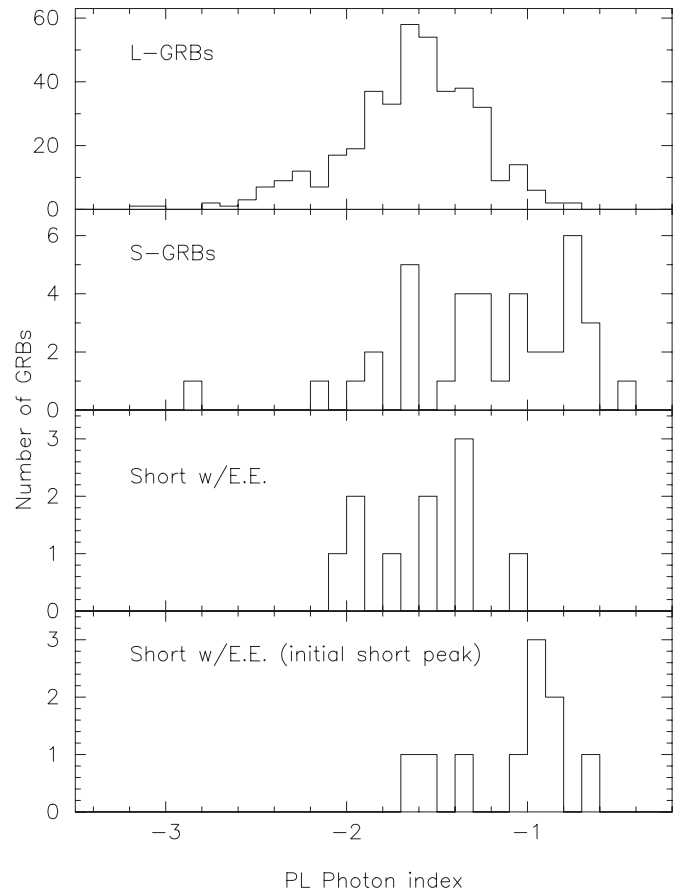


Figure 13. From top to bottom: histograms of the BAT time-averaged photon index for a PL fit for the L-GRBs, the S-GRBs, the S-GRBs with E.E., and the initial short spikes of the S-GRBs with E.E.

4.6. Time-resolved Spectral Parameters

We have chosen 3284 out of 3323 time-resolved spectra, for further study, based on the goodness of fit ($\chi^2_{\nu} < 2$) and also the constraints on the spectral parameters. Figure 17 compares the distributions of the photon index in a PL fit between the time-resolved and the time-averaged spectral samples. Fitting a Gaussian to each of the histograms gives for the time-resolved sample a peak at -1.53 with σ of 0.47 and for the time-averaged sample a peak at -1.57 with σ of 0.32. The K-S test probability for the time-resolved and the time-averaged PL photon index distribution is 10^{-4} . Therefore, there is a marginal difference in the photon index of a PL fit between the time-resolved and the time-averaged spectra, especially in the widths of their distributions.

Figure 18 shows the differences in $E_{\text{peak}}^{\text{obs}}$ from the CPL fit between the time-resolved and the time-averaged spectra. Four hundred and seventy-two out of 3284 time-resolved spectra show a significant improvement of χ^2 in a CPL fit over a PL fit ($\Delta\chi^2 > 6$). The Gaussian fits to these log-normal $E_{\text{peak}}^{\text{obs}}$ histograms show a peak at 68 keV with $\log(E_{\text{peak}}^{\text{obs}})$ of 0.23 for the time-resolved sample and a peak at 77 keV with $\log(E_{\text{peak}}^{\text{obs}})$ of 0.19 for the time-averaged spectra. We found a K-S probability of 0.04 for the comparison in $E_{\text{peak}}^{\text{obs}}$ distributions between the time-resolved and the time-averaged spectra. Therefore, there is no significant difference in $E_{\text{peak}}^{\text{obs}}$ based on a CPL fit between the BAT time-resolved and the time-averaged spectra.

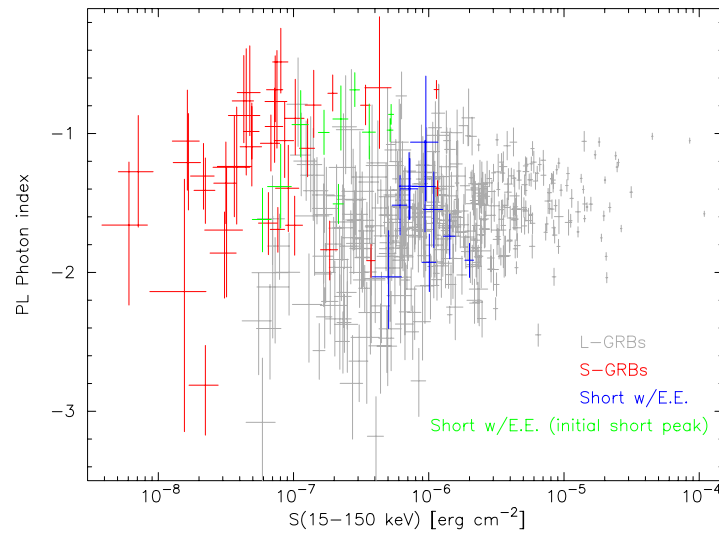


Figure 14. Distribution of the BAT PL photon index vs. the energy fluence in the 15–150 keV band for the L-GRBs (light gray), the S-GRBs (red), the S-GRBs with E.E. (blue), and the initial short spikes of the S-GRBs with E.E. (green).
(A color version of this figure is available in the online journal.)

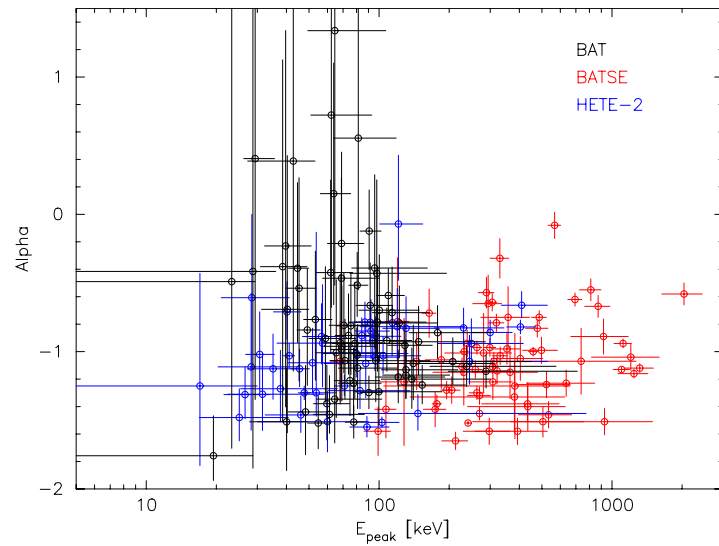


Figure 15. Distributions of the photon index α and E_{peak} in a CPL fit for the BAT (black), the BATSE (red), and the *HETE-2* (blue) GRBs.
(A color version of this figure is available in the online journal.)

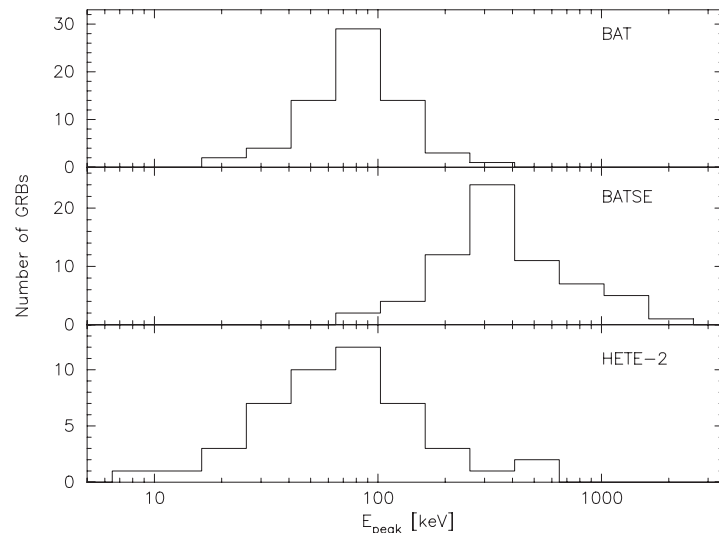


Figure 16. Histograms of E_{peak} in a CPL fit for the BAT (top), the BATSE (middle), and the *HETE-2* (bottom) GRBs.

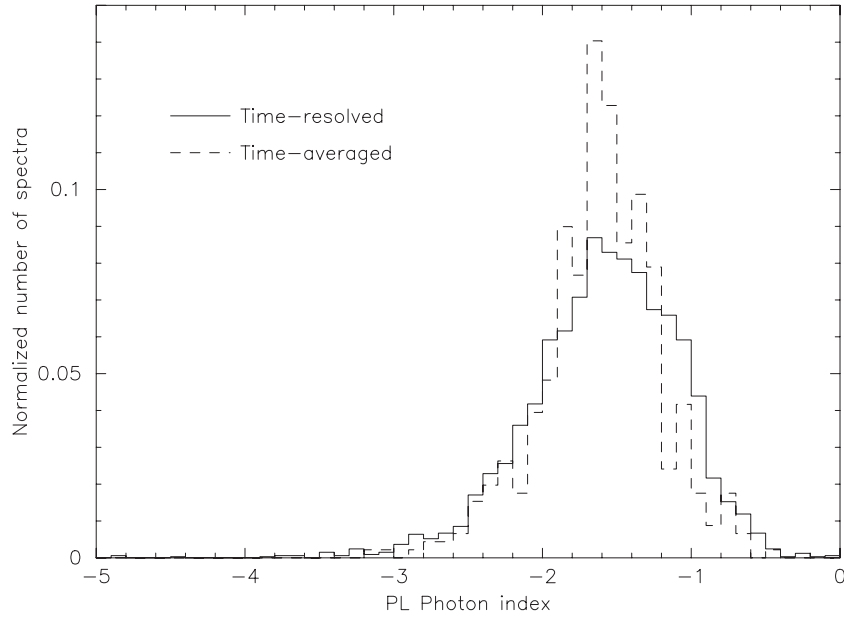


Figure 17. Histograms of the BAT photon index in a PL fit for the time-resolved (solid) and the time-averaged (dash) spectra. The histograms are normalized by the total number of spectra in each sample.

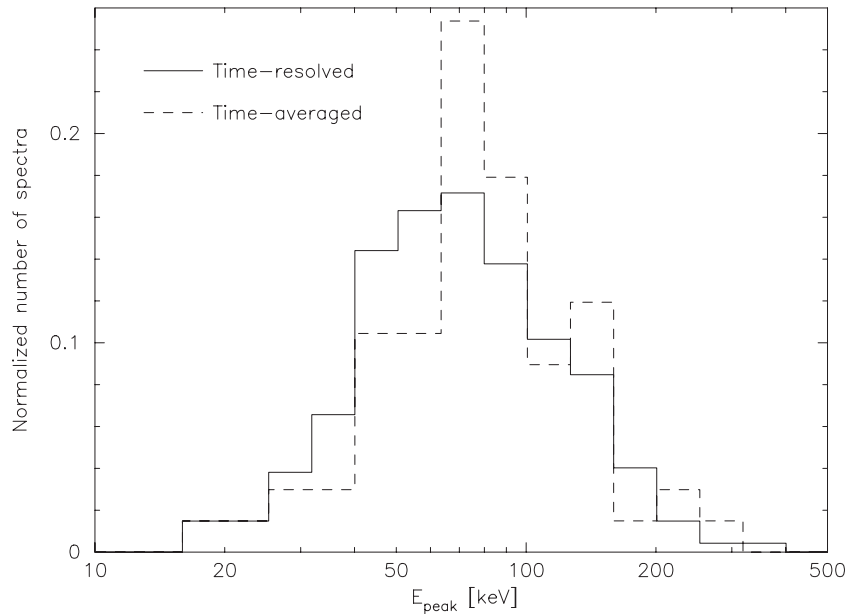


Figure 18. Histograms of the BAT E_{peak} in a CPL fit for the time-resolved (solid) and the time-averaged (dashed) spectra. The histograms are normalized by a total number of spectra.

Ghirlanda et al. (2009) suggested a possible resemblance between the low-energy photon index α of the S-GRBs and the initial part of the spectrum of the L-GRBs in the BATSE GRBs. Figure 13 shows a significant difference in the time-averaged photon index for a PL fit in the BAT data between the L-GRBs and the S-GRBs. Therefore, it is worth investigating this difference using our time-resolved spectral results. Figure 19 shows the histograms of the BAT photon index in a PL fit for the initial spectra of the L-GRBs and the time-averaged photon index of the S-GRBs. The initial spectrum is chosen to be the first spectrum of the time-resolved spectra for each burst. The K-S test probability comparing the initial PL photon indices of the L-GRBs and the time-averaged photon indices of the S-GRBs is 0.02. Therefore, the K-S test shows no clear indication that the PL photon indices in the initial intervals of the L-GRBs

and the time-averaged PL photon indices of the S-GRBs are drawn from the same parent population in the BAT data.

One of the important questions about prompt emission from GRBs is whether or not the observed spectrum is correctly represented by the synchrotron shock model (SSM; Rees & Mészáros 1992; Sari et al. 1998). According to Preece et al. (1998), 23% of the BATSE time-resolved spectra have low-energy photon indices which violate the SSM limit from $-3/2$ to $-2/3$ (the so-called line of death problem). Although the BAT photon index based on a PL fit does not represent the low-energy photon index α of the Band function if $E_{\text{peak}}^{\text{obs}}$ is located inside the BAT energy range (see Section 4.5), the BAT photon index should be the actual low-energy photon index α if $E_{\text{peak}}^{\text{obs}}$ is located above the BAT energy range. Therefore, the photon index derived from a PL fit in the BAT time-resolved spectra is

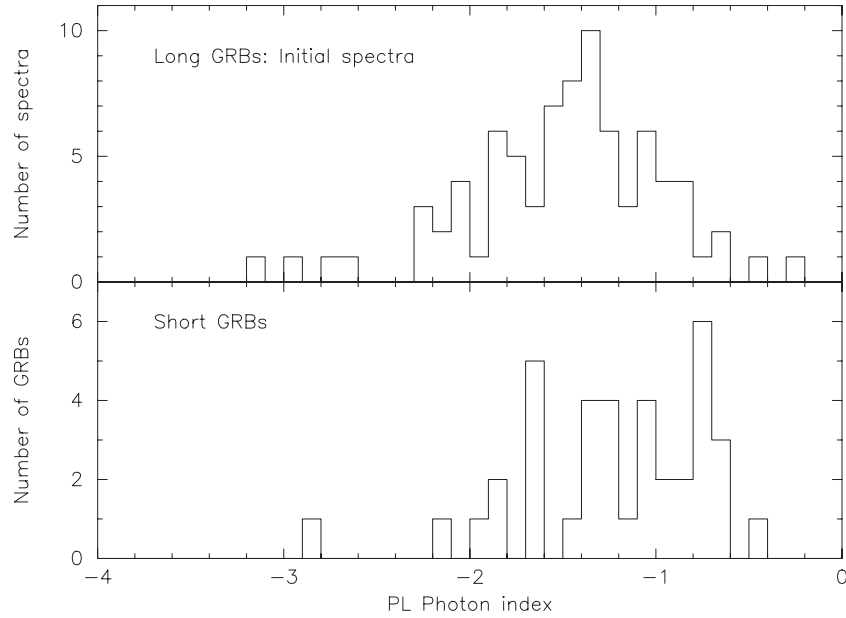


Figure 19. Histograms of the BAT photon index in a PL fit for initial spectra of long GRBs (top) and for short GRBs (bottom).

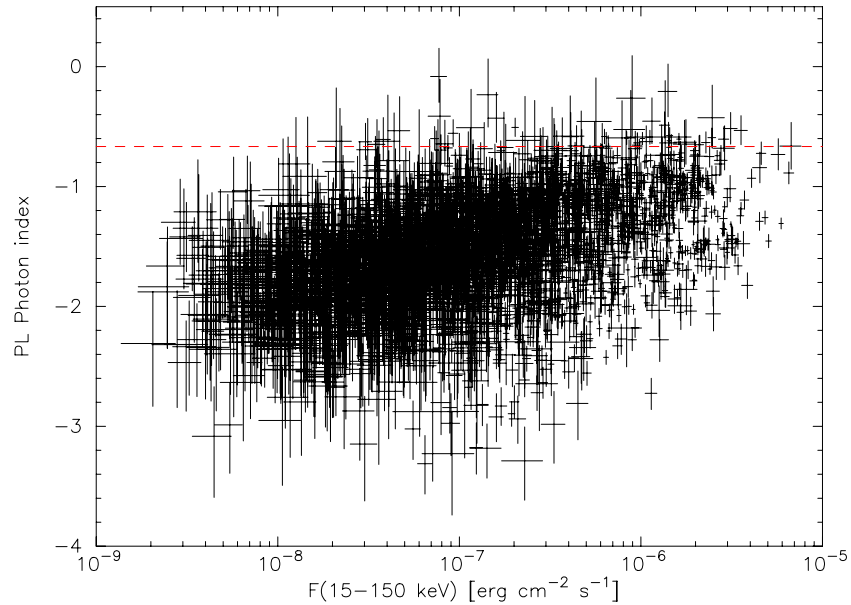


Figure 20. Distribution of the BAT photon index in a PL fit vs. energy flux in the 15–150 keV band. The red dashed line shows the photon index of $-2/3$. The total number of time-resolved spectra in this plot is 2968.

(A color version of this figure is available in the online journal.)

the interesting data set to investigate the line of death problem. Figure 20 shows the BAT photon index versus the energy flux in the 15–150 keV band using time-resolved spectra with a PL fit. We only used the results for which the 90% error of the photon index has been constrained within ± 0.5 . Out of 2968 points in the figure, 18 spectra (0.6%) exceed the hard side of the line of death ($> -2/3$) by $> 1.6\sigma$ level. Figure 21 shows the distribution of the low-energy photon index α versus $E_{\text{peak}}^{\text{obs}}$ of the BAT time-resolved spectra for which there is a significant improvement of χ^2 in a CPL fit over a PL fit. Just as in the PL fit samples, we only used spectra where the low-energy photon index α is constrained within ± 0.5 at the 90% confidence level. The low-energy photon index of 23 out of 234 spectra is harder than $-2/3$ by $> 1.6\sigma$ level. There is only one time-resolved spectrum

(GRB 090618 from 110.5 s to 112.272 s from the trigger time) which violates the softer side of the line of death ($< -3/2$) at the significance level of $> 1.6\sigma$. Therefore, the total fraction of the BAT spectra in the CPL samples which violate either line of death is $\sim 10\%$. Although there are the spectra which violate the line of death in the BAT data, it is likely that the number of the BAT spectra which violate the limit is a factor of two smaller than the BATSE result. Figure 22 show the BAT light curves with shading of the time intervals exceeding the line of death. We note that the intervals exceeding the line of death are mostly in bright spikes in the light curves. Furthermore, in some bursts, the rising part of the light curve (e.g., GRB 080319B) exceeds the limit. Although it is hard to conclude which part of the light curve violates the line of death because of the small

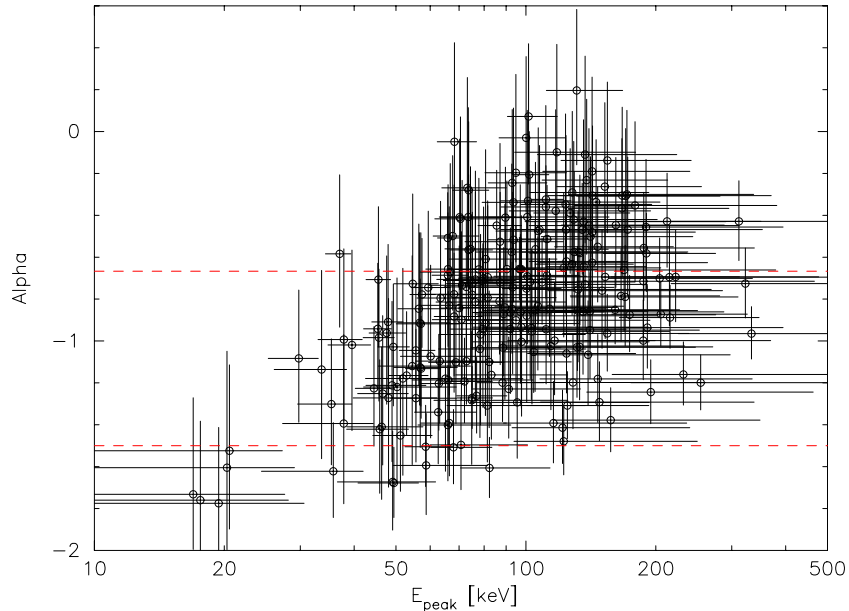


Figure 21. Distribution of the BAT photon index α vs. E_{peak} in a CPL fit. The red dashed lines show the photon index region from $-3/2$ to $-2/3$. The total number of time-resolved spectra in this plot is 234.

(A color version of this figure is available in the online journal.)

number of samples in our study, we do see a general trend that (1) a bright peak and (2) a rising part of a peak in the light curve tend to exceed the line of death limit. This is consistent with the BATSE results that the initial part of the FRED pulses tends to violate the line of death (Lu et al. 2010). However, we do want to stress that majority of the photon indices derived from the BAT spectra are consistent with the expectation of the SSM.

An interesting result from the *Fermi* mission is that in at least one burst, GRB 090902B (Abdo et al. 2009), which has a strong GeV detection by the Large Area Telescope shows the presence of an underlying PL component in addition to a Band function component in the time-resolved spectra. The extra PL component emerges not only in the GeV energy range but also in the <50 keV energy range. We decided to investigate, whether such a feature is present as well in the BAT time-resolved spectra. To do this, we perform BAT spectral simulations using the spectral parameters of the interval b of GRB 090902B (from 4.6 s to 9.6 s) as reported in Abdo et al. (2009): the Band function parameters of $\alpha = 0.07$, $\beta = -3.9$, and $E_{\text{peak}}^{\text{obs}} = 908$ keV, and the extra PL photon index of -1.94 . We simulate 10,000 spectra using the BAT energy response of 30° off-axis with the `xspec fakeit` command. The background from the real data is included in the simulation. When then checked to see how well the two models, PL and CPL, fit the simulated spectra. Figure 23 shows one example of a simulated spectrum fitted by a PL model. Since the input spectrum has a steep PL (photon index of -1.94) and then breaks to a very flat PL (photon index of 0.07) around 50 keV, the BAT-simulated spectrum shows a significant deviation from a PL fit. In this example, the reduced χ^2 in a PL fit is 2.93. Figure 24 shows the reduced χ^2 distribution of all the BAT simulated spectra when fitted by a PL model. A Gaussian fit to this histogram yields a peak of 2.58 with σ of 0.28. 99.97% of the simulated spectra show a reduced $\chi^2 \geq 1.7$. None of the CPL fits to the simulated spectra shows a significant improvement over a PL fit. By comparison when we look at the real BAT spectra, we find that the reduced χ^2

distributions of the time-averaged and the time-resolved spectra fitted either by a PL or a CPL model are well centered around 1 (Figure 25). There are only two time-resolved spectra (out of 3284) which show a reduced $\chi^2 > 1.7$. For these two spectra, the residuals from the best-fit models are not similar to the residuals seen in Figure 24. For the time-averaged spectra, the poorest reduced χ^2 is 1.54. We can therefore conclude that we do not confirm the existence of an extra PL component which extends below 50 keV in the BAT GRB spectra. Although GRB 090902B and other *Fermi* GRBs for which detections of the extra PL component are claimed could be a special type of GRB which has never been observed by the BAT, we believe that confirmations from other GRB instruments are required to validate the existence of the extra PL component and especially its presence in the hard X-ray range of the spectrum.

4.7. Observed Properties versus Redshifts

Figure 26 shows the observed BAT T_{90} duration versus redshift. We also plot the calculated T_{90} that we would observe if three particular GRBs, GRB 050525A ($z = 0.606$), GRB 061126 ($z = 1.1588$), and GRB 061222B ($z = 3.355$) had occurred at different redshifts. If high- z bursts have the same duration distribution in the rest frame as low- z bursts, then we would expect the duration of a high-redshift GRB tends to be longer as shown in the trajectories. Due to the intrinsic scatter in duration and also the relatively small number of high-redshift GRBs, it is difficult to conclude whether we see a clear indication of the time-dilation effect in the data.

Figure 27 shows the observed photon index of the time-averaged spectra in a PL fit versus redshift. If there is an intrinsic spectral shape in the GRB rest frame, we would expect the observed spectra to be softer when the redshift is higher. The overlaid curves in the figure show the expected BAT observed

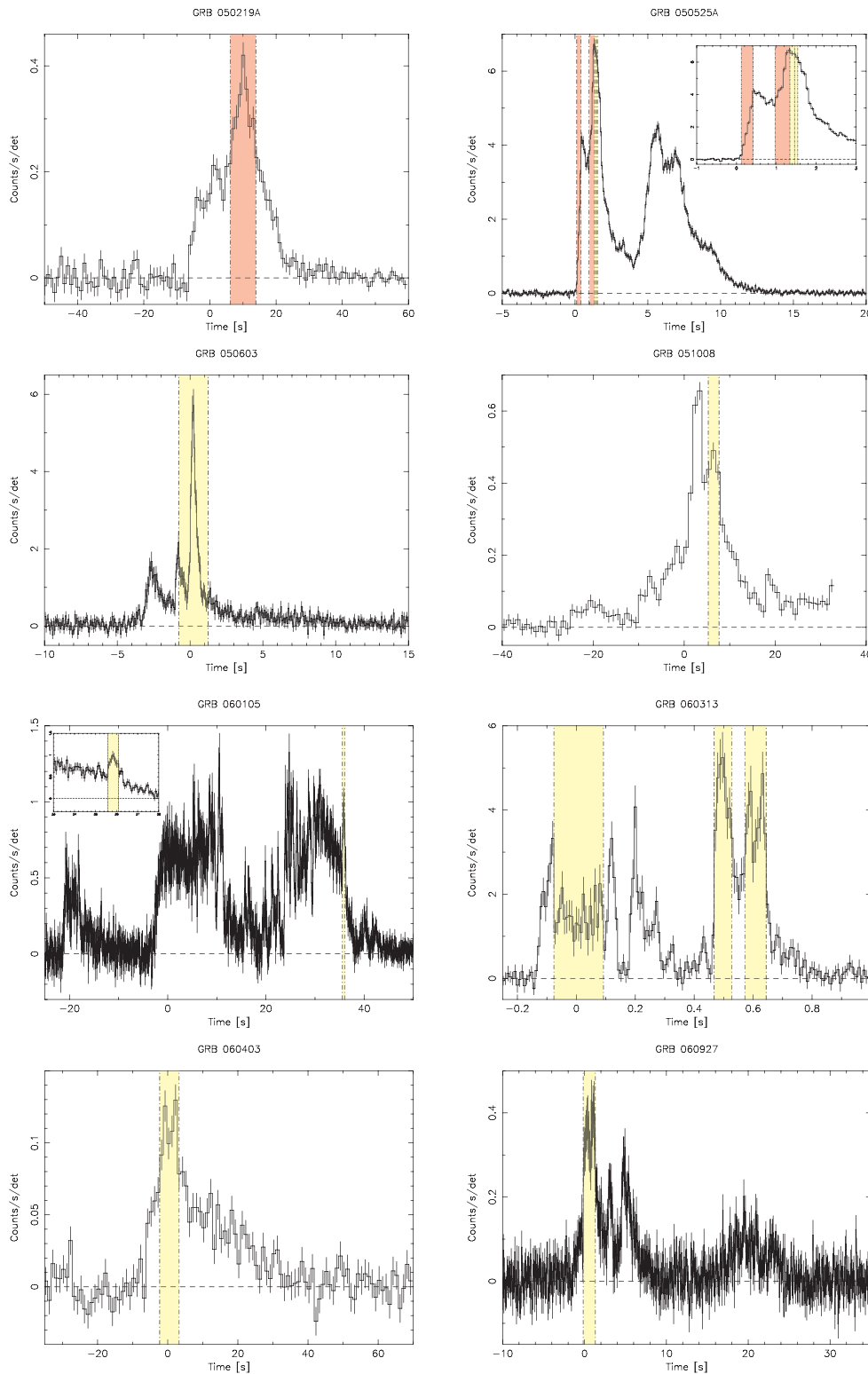


Figure 22. BAT light curves with the intervals for which the spectra exceed the limits of the SSM as shaded. The red shading indicates intervals exceeding the limit by $> 3.2\sigma$. The yellow shading indicates intervals exceeding the limit by $> 1.6\sigma$. (A color version of this figure is available in the online journal.)

PL photon index as a function of redshift for a model burst with $E_{\text{peak}}^{\text{src}}$ of 300 keV, 100 keV, and 30 keV. We used the $E_{\text{peak}}-\Gamma$ relation (Sakamoto et al. 2009) to convert $E_{\text{peak}}^{\text{obs}}$ into the BAT PL photon index for these curves. There is no obvious trend because of the intrinsic scatter in the data and relatively small sample of high-redshift GRBs.

The distributions of the peak flux and the fluence as a function of redshift are shown in Figures 28 and 29. Although the peak flux and the fluence measured in the narrow BAT energy band are not bolometric measurements, there is no obvious correlation between those parameters and the redshifts. The fluence and the peak flux of the low-redshift GRBs are scattered from the lowest

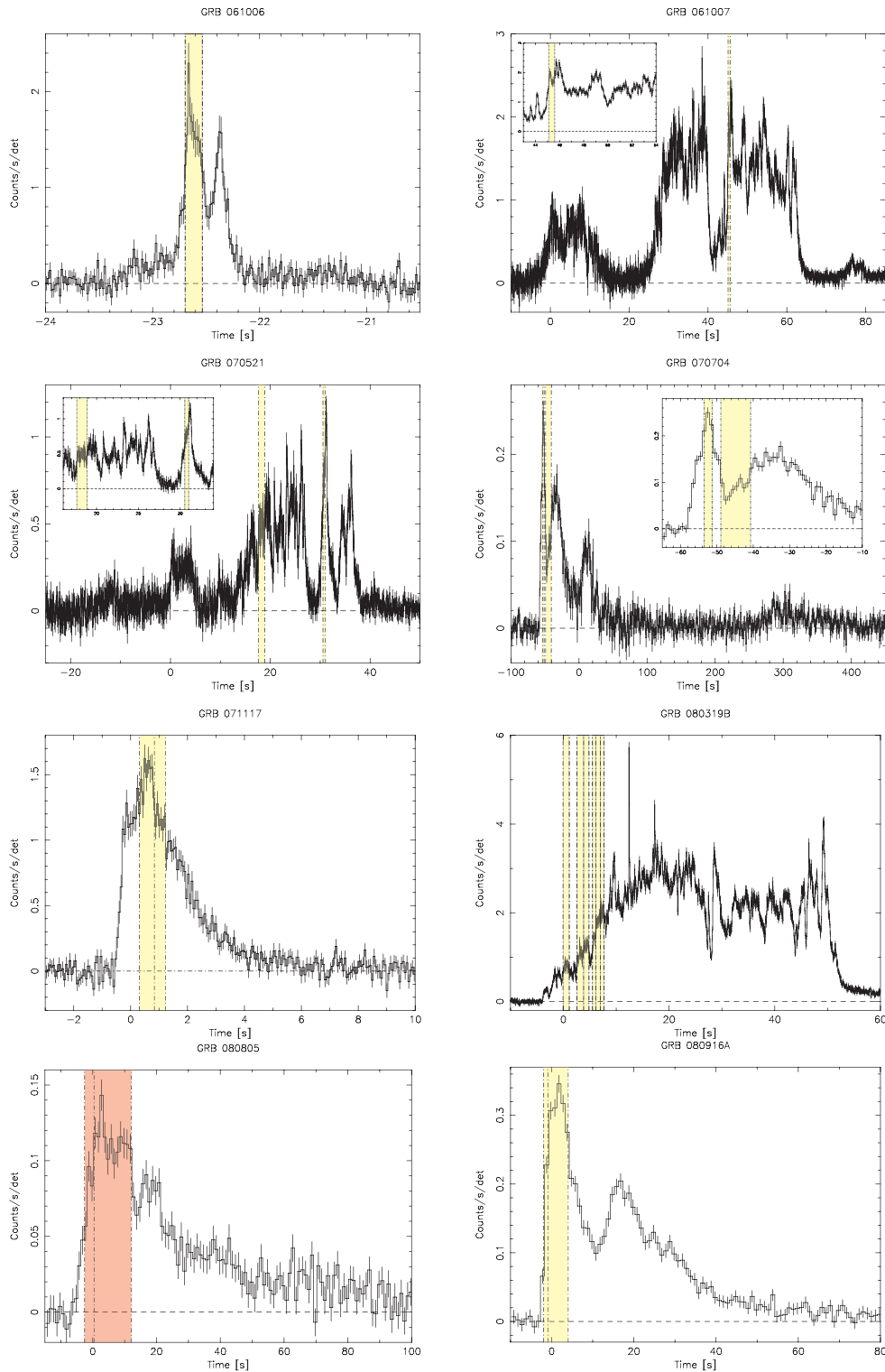


Figure 22. (Continued)

to the highest values. The high-redshift GRBs are located in the small peak flux and the fluence region, but they are not the dimmest populations of the BAT known redshift GRBs.

4.8. Rest-frame Properties

Figure 30 shows the distribution of T_{90} and T_{50} durations calculated in the 140–220 keV band in the GRB rest frame as a function of redshift. The averaged T_{90} and T_{50} durations in

the rest frame are 18.5 s and 8.0 s, respectively. The respective correlation coefficients between T_{90} and T_{50} and the redshifts are 0.09 in 122 samples (null probability of 0.3) and 0.1 in 121 samples (null probability of 0.3). Therefore, there is no clear trend between the duration in the GRB rest frame and the redshift.

Figure 31 shows the correlation between $E_{\text{peak}}^{\text{src}}$ and the isotropic-equivalent energy E_{iso} . The $E_{\text{peak}}^{\text{src}}$ and E_{iso} values of

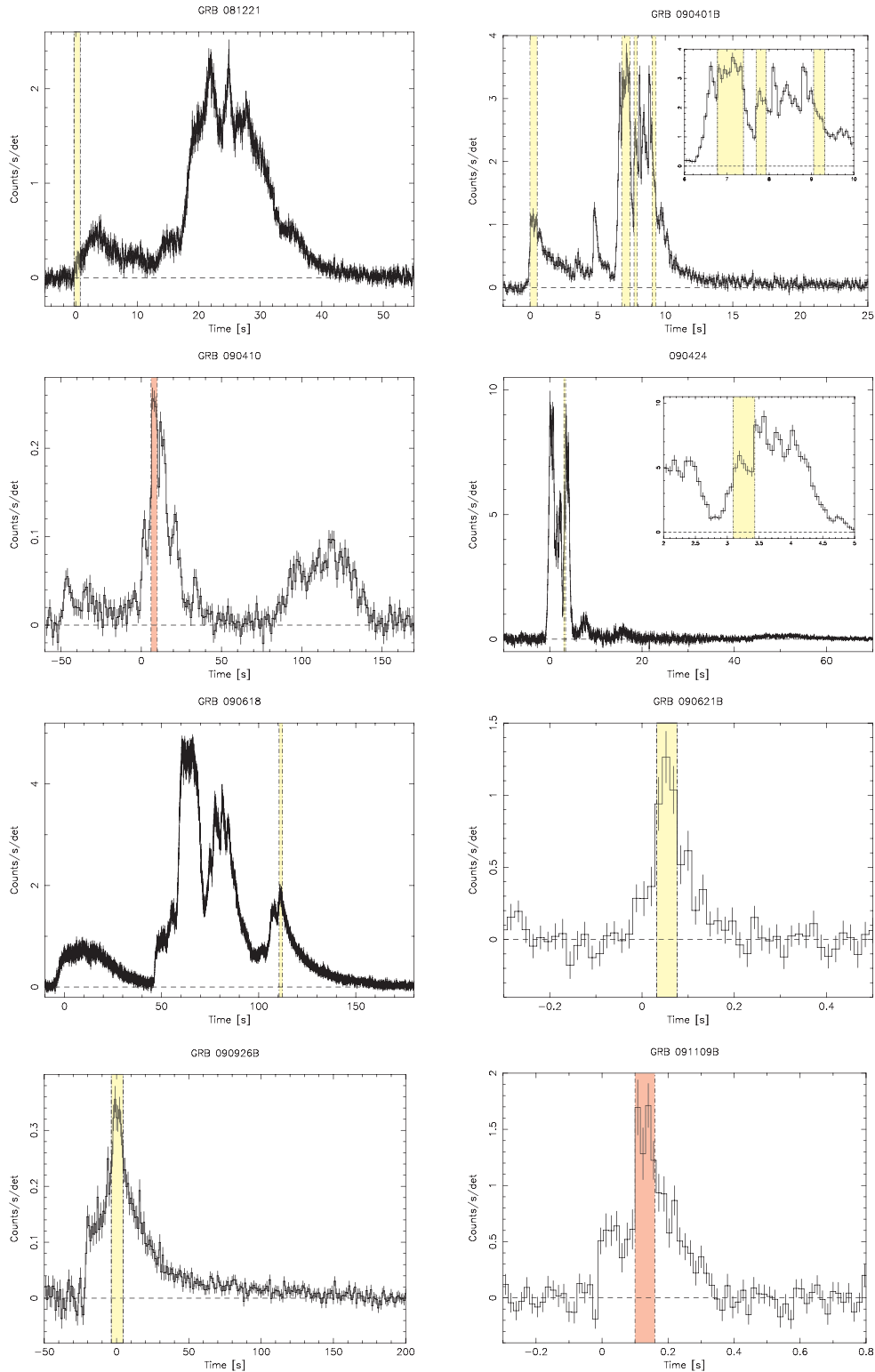


Figure 22. (Continued)

the GRB samples from BATSE, *BeppoSAX*, and *HETE-2* are extracted from Amati (2006). We only select the *Swift* GRBs for which we reported the time-averaged CPL fits in this catalog and that also have redshift measurements. For those bursts, we fit the spectrum with a Band function to measure $E_{\text{peak}}^{\text{src}}$ and E_{iso} . E_{iso} is calculated by integrating over the 1 keV–10 MeV

band in the GRB rest frame. We used the same cosmological parameters of Amati (2006) in the calculation of E_{iso} for the *Swift* GRBs. Table 13 summarizes the values of $E_{\text{peak}}^{\text{src}}$ and E_{iso} of *Swift* GRBs. As shown in Figure 31, the *Swift* GRB samples are consistent with the samples from other GRB missions and follow the relation originally proposed by Amati et al. (2002).

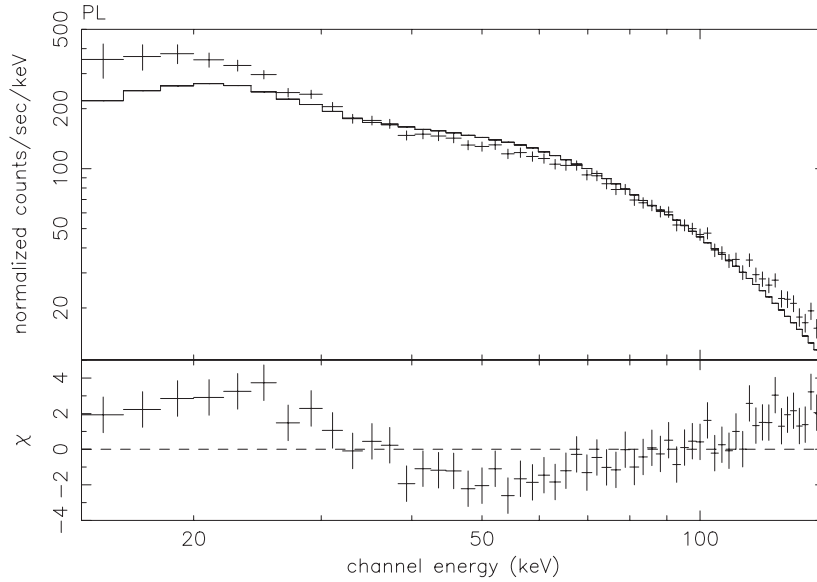


Figure 23. Simulated BAT spectrum with a Band function plus an additional power-law component (see the text). The solid line shows a fit to a PL model.

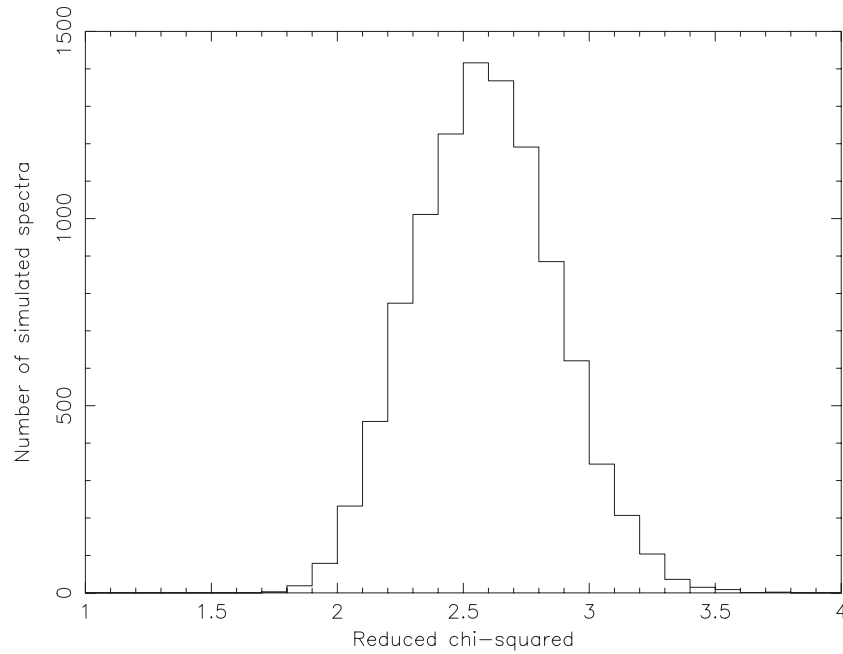


Figure 24. Histogram of reduced χ^2 in a PL fit of 10,000 BAT simulated spectra of the *Fermi* GRB 090902B interval b spectral parameters as the input spectrum.

5. SUMMARY

The BAT2 catalog includes 476 GRBs detected by BAT during five years of operation. We present the observed temporal and spectral properties of the BAT GRBs mainly based on BAT event data. In this catalog, we present not only the time-averaged but also the time-resolved spectral properties of the BAT GRBs. We also distinguish among L-GRBs, S-GRBs, and S-GRBs with E.E. to investigate possible distinct characteristics in the prompt emission properties. Comparisons of the prompt emission properties among the BATSE, the *BeppoSAX*, and the *HETE-2* GRB samples are shown. The observed prompt emission properties for the BAT known redshift GRBs are also presented.

We have shown that the BAT T_{90} and T_{50} durations peak around 70 s and 30 s, respectively, whereas the BATSE, the

BeppoSAX, and the *HETE-2* T_{90} durations peak around 10–30 s. This can be understood by the differences in the sensitivities of the instruments. We have confirmed that the spectra of the BAT S-GRBs are generally harder than those of the L-GRBs. The overall hardness of the S-GRBs with E.E. is comparable to that of the L-GRBs, whereas the hardness of the initial short spikes of the S-GRBs with E.E. is comparable to that of the S-GRBs. By comparing the BAT GRBs with the BATSE and the *HETE-2* samples using the fluences in the 50–150 keV and the 15–50 keV bands, we have shown that the majority of the BAT GRBs are systematically softer than the bright BATSE GRBs, whereas the *HETE-2* samples overlap with the BAT GRBs in this fluence–fluence plane. We have confirmed that the photon indices of PL fits to the BAT S-GRBs are harder than those of the L-GRBs in the time-averaged spectral analysis. The distribution of the time-averaged PL photon indices of the S-GRBs with

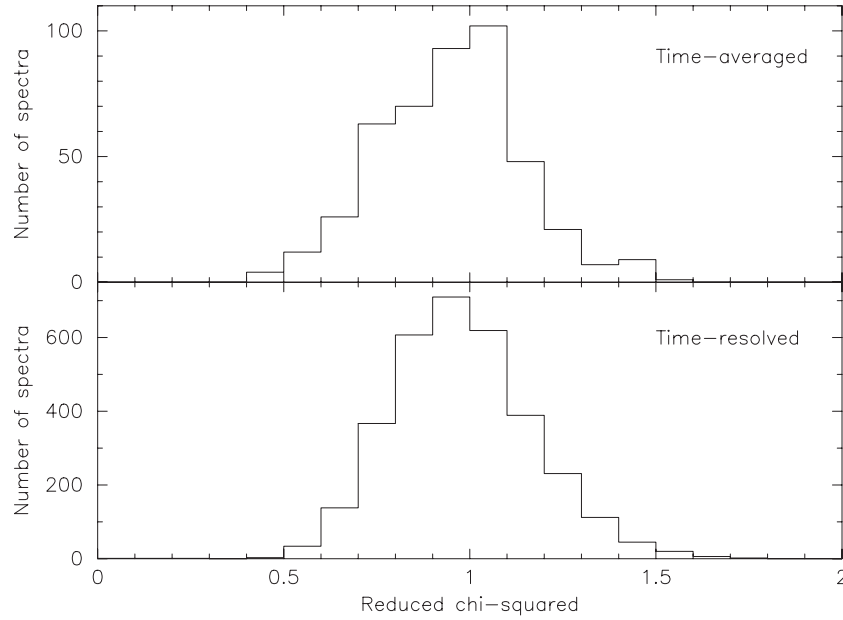


Figure 25. Histogram of reduced χ^2 in the best-fit model (either a PL or a CPL model) for the real time-averaged spectra (top) and the time-resolved spectra (bottom). The Gaussian fits to these histograms show, respectively, peaks of 0.95 with a σ of 0.19 and 0.96 with a σ of 0.18.

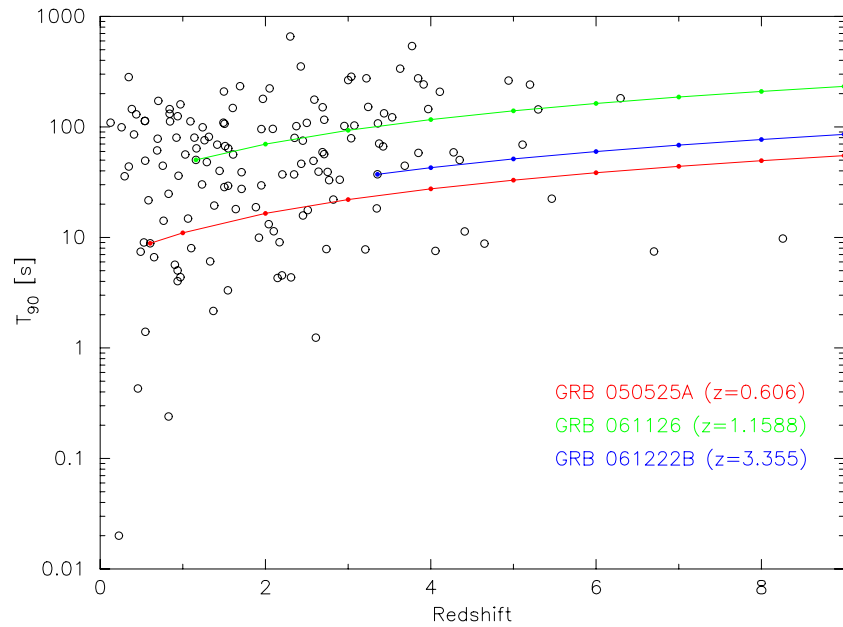


Figure 26. Distribution of the BAT observed T_{90} vs. redshift. For three known redshift GRBs, GRB 050525A ($z = 0.606$), GRB 061126 ($z = 1.1588$), and GRB 061222B ($z = 3.355$), we calculated the trajectories of estimated observed T_{90} as a function of redshift assuming that the duration changes only by the time-dilation effect.

(A color version of this figure is available in the online journal.)

E.E. is consistent with that of the L-GRBs. However, the PL photon indices of the initial short spikes of the S-GRBs with E.E. are much more similar to those of the S-GRBs. The time-averaged $E_{\text{peak}}^{\text{obs}}$ of the BAT GRBs based on a CPL fit shows a log-normal distribution in the peak around 80 keV which is significantly smaller than that of the BATSE GRBs which peak around 320 keV. There is no significant difference in the $E_{\text{peak}}^{\text{obs}}$ based on a CPL fit between the time-averaged and the time-resolved spectra in the BAT data. We have confirmed that only 10% of the BAT photon indices in the BAT time-resolved spectra are outside the allowed range of the line of death (the limit from the SSM). The intervals that violate the line of death

are at bright peaks and/or at a rising part of a peak. We see no obvious observed trend in the BAT T_{90} and the observed spectra with redshifts. The T_{90} and T_{50} durations calculated in the 140–220 keV band in the GRB rest frame for the BAT known redshift sample are peaked at 19 s and 8 s, respectively. The BAT GRB samples are consistent with the $E_{\text{peak}}^{\text{src}} - E_{\text{iso}}$ relation (Amati relation).

We thank C. R. Shrader for instructing tools (CGRO ftools) to read BATSE data by xspec. We also thank the anonymous referee for comments and suggestions that materially improved the paper.

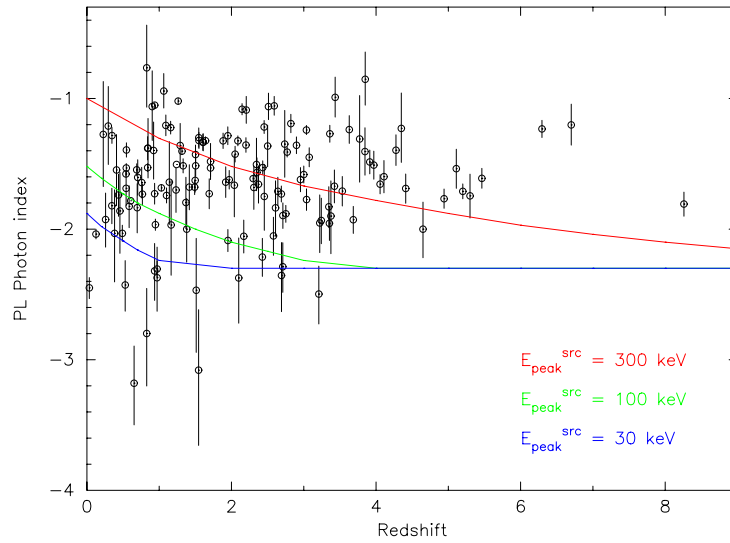


Figure 27. Distribution of the BAT observed PL photon index vs. redshift. The overlaid curves are the estimates of the BAT observed PL photon index as a function of redshift assuming the intrinsic spectrum is the redshifted spectrum of the typical Band function shape ($\alpha = -0.87 \pm 0.33(1\sigma)$ and $\beta = -2.36 \pm 0.31(1\sigma)$; see Sakamoto et al. 2009) with the rest-frame E_{peak} of 300 keV (red), 100 keV (green), and 30 keV (blue).

(A color version of this figure is available in the online journal.)

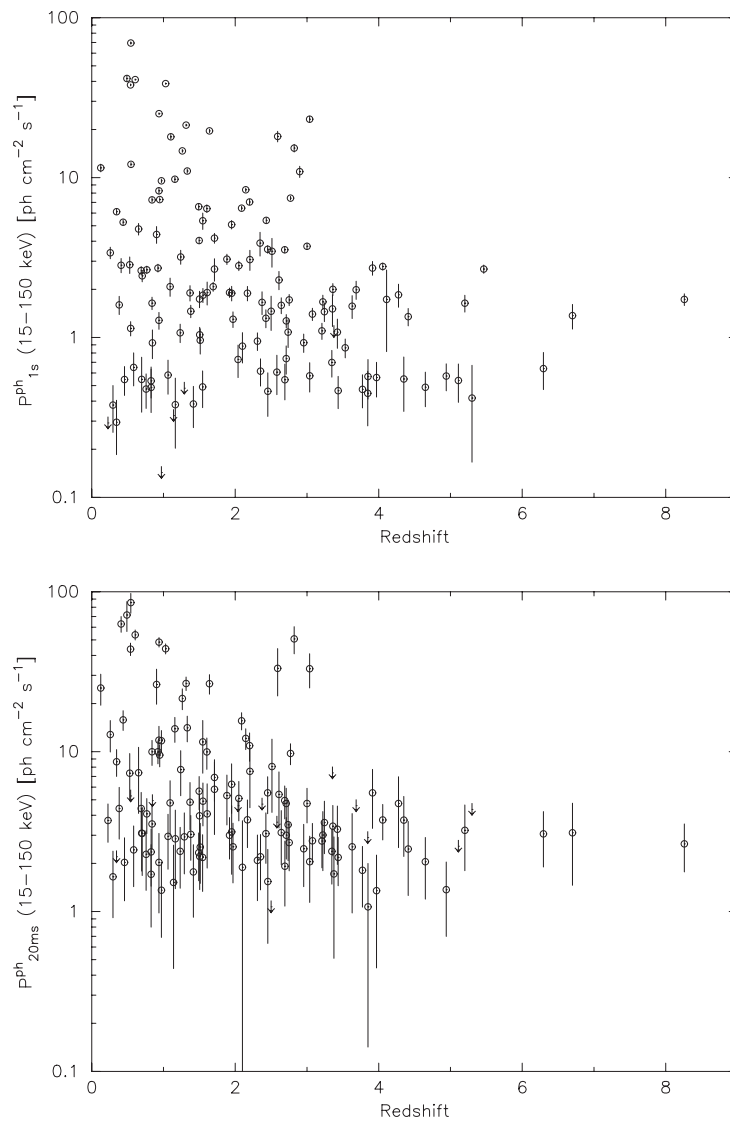


Figure 28. Distribution of 1 s (top) and 20 ms (bottom) observed peak photon flux in the 15–150 keV band vs. redshift.

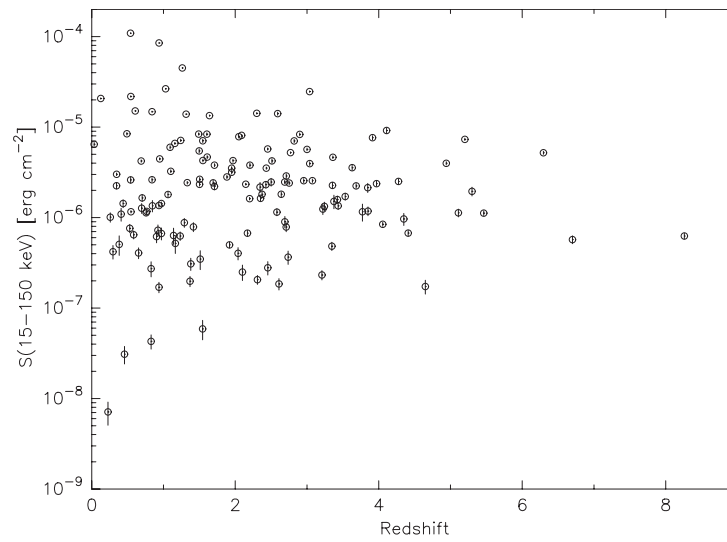


Figure 29. Distribution of the BAT observed energy fluence in the 15–150 keV band vs. redshift.

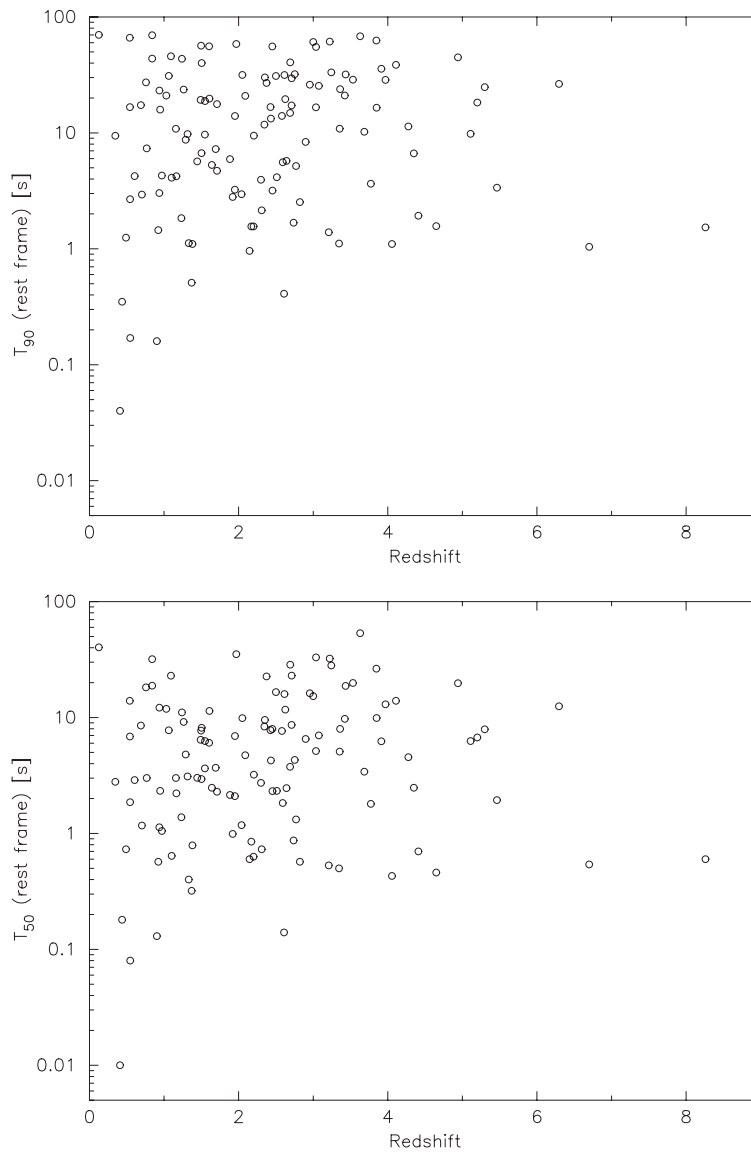


Figure 30. Distributions of T_{90} (top) and T_{50} (bottom) in the 140–220 keV band at the GRB rest frame vs. redshift.

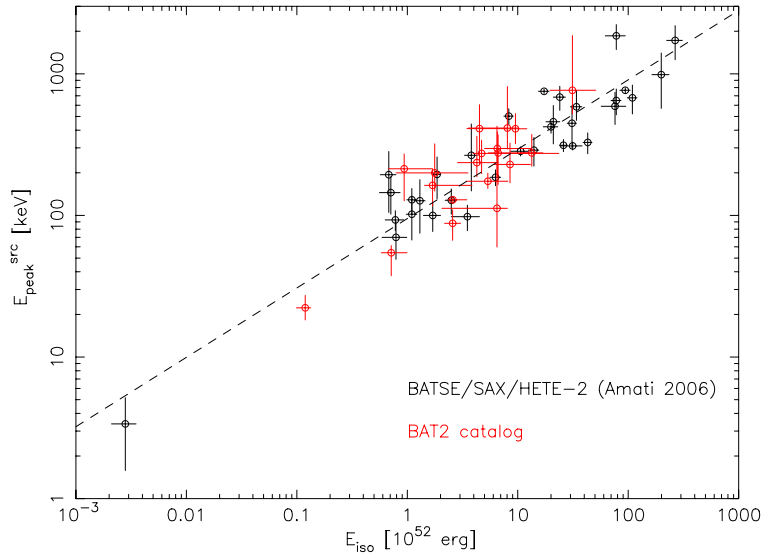


Figure 31. Correlation between $E_{\text{peak}}^{\text{src}}$ and E_{iso} for the *Swift* GRBs (red) and other GRB missions (black). The dashed line is the best-fit correlation between $E_{\text{peak}}^{\text{src}}$ and E_{iso} reported by Amati (2006): $E_{\text{peak}}^{\text{src}} = 95 \times (E_{\text{iso}}/10^{52})^{0.49}$.

(A color version of this figure is available in the online journal.)

Table 13
 $E_{\text{peak}}^{\text{src}}$ and E_{iso} Values for *Swift* GRBs

| GRB | z | $E_{\text{peak}}^{\text{src}}$ (keV) | E_{iso} (10^{52} erg) |
|---------|--------|---|--------------------------------------|
| 050416A | 0.6528 | 22^{+5}_{-4} | $0.12^{+0.01}_{-0.02}$ |
| 050525A | 0.606 | 129^{+6}_{-7} | $2.6^{+0.9}_{-0.2}$ |
| 060115 | 3.5328 | 297^{+92}_{-111} | $6.5^{+6.7}_{-1.5}$ |
| 060206 | 4.0559 | 410^{+195}_{-179} | $4.5^{+3.2}_{-1.0}$ |
| 060707 | 3.4240 | 274^{+66}_{-77} | $4.7^{+18.8}_{-0.8}$ |
| 060908 | 1.8836 | 414^{+399}_{-120} | $8.1^{+1.9}_{-4.5}$ |
| 060927 | 5.4636 | 276^{+97}_{-54} | 13^{+3}_{-3} |
| 071010B | 0.947 | 88^{+21}_{-21} | $2.6^{+0.5}_{-0.4}$ |
| 071117 | 1.3308 | 112^{+315}_{-52} | $6.5^{+1.6}_{-4.4}$ |
| 080413B | 1.1014 | 163^{+51}_{-46} | $1.7^{+2.2}_{-0.3}$ |
| 080603B | 2.6892 | 277^{+95}_{-111} | $6.6^{+6.2}_{-1.2}$ |
| 080605 | 1.6403 | 766^{+1100}_{-243} | 31^{+20}_{-12} |
| 080916A | 0.6887 | 200^{+120}_{-51} | $1.8^{+1.8}_{-1.0}$ |
| 090205 | 4.6497 | 214^{+58}_{-87} | $0.9^{+0.7}_{-0.3}$ |
| 090423 | 8.26 | 410^{+115}_{-88} | $9.5^{+2.6}_{-1.9}$ |
| 090424 | 0.544 | 236^{+127}_{-49} | $4.3^{+2.4}_{-1.4}$ |
| 090926B | 1.24 | 175^{+24}_{-20} | $5.4^{+2.8}_{-2.0}$ |
| 091018 | 0.971 | $55^{+6.8}_{-17}$ | $0.7^{+0.3}_{-0.1}$ |
| 091029 | 2.752 | 229^{+94}_{-59} | $8.5^{+4.5}_{-2.5}$ |

REFERENCES

- Abdo, A. A., et al. 2009, *ApJ*, 706, L128
 Amati, L. 2006, *MNRAS*, 372, 233
 Amati, L., et al. 2002, *A&A*, 390, 81
 Atteia, J.-L., et al. 2003, in AIP Conf. Proc. 662, Gamma-Ray Bursts and Afterglow Astronomy 2001, ed. G. R. Ricker & R. K. Vanderspek (Melville, NY: AIP), 17
 Band, D. L., et al. 1993, *ApJ*, 413, 281
 Barthelmy, S. D., et al. 2005a, *Space Sci. Rev.*, 120, 143
 Barthelmy, S. D., et al. 2005b, *Nature*, 438, 994
 Berger, E. 2009, *ApJ*, 690, 231
 Berger, E., & Becker, G. 2005, GCN Circ., 3520, <http://gcn.gsfc.nasa.gov/gcn3/3520.gcn3>
 Berger, E., Penprase, B. E., Cenko, S. B., Kulkarni, S. R., Fox, D. B., Steidel, C. C., & Reddy, N. A. 2006, *ApJ*, 642, 979
 Berger, E., et al. 2005a, *ApJ*, 629, 328
 Berger, E., et al. 2005b, *ApJ*, 634, 501
 Berger, E., et al. 2005c, *Nature*, 438, 988
 Burrows, S. D., et al. 2005, *Space Sci. Rev.*, 120, 165
 Copete, A., Grindlay, J., Hong, J., Barthelmy, S., & Gehrels, N. 2007, GCN Circ. 6653, <http://gcn.gsfc.nasa.gov/gcn3/6653.gcn3>
 Della Valle, M., et al. 2006, *ApJ*, 642, L103
 Evans, P. A., et al. 2009, *MNRAS*, 397, 1177
 Fenimore, E. E., in 't Zand, J. J. M., Norris, J. P., Bonnel, J. T., & Nemiroff, R. J. 1995, *ApJ*, 448, L101
 Frontera, F., et al. 2009, *ApJS*, 180, 192
 Fynbo, J. P. U., et al. 2009, *ApJS*, 185, 526
 Gehrels, N., et al. 2004, *ApJ*, 611, 1005
 Gehrels, N., et al. 2005, *Nature*, 437, 851
 Ghirlanda, G., Nava, L., Ghisellini, G., Celotti, A., & Firmani, C. 2009, *A&A*, 496, 585
 Jakobsson, P., et al. 2006, *A&A*, 447, 897
 Jung, G. V. 1989, *ApJ*, 338, 972
 Kaneko, Y., Preece, R. D., Briggs, M. S., Paciesas, W. S., Meegan, C. A., & Band, D. L. 2006, *ApJS*, 166, 298
 Kawai, N., et al. 2006, *Nature*, 440, 184
 Kouveliotou, C., Meegan, C. A., Fishman, G. J., Bhat, N. P., Briggs, M. S., Koshut, T. M., Paciesas, W. S., & Pendleton, G. N. 1993, *ApJ*, 413, L101
 Lu, R.-J., Hou, S.-J., & Liang, E.-W. 2010, *ApJ*, 720, 1146
 Mirabal, N., Halpern, J. P., & O'Brien, P. T. 2007, *ApJ*, 661, L127
 Norris, J. P., Gehrels, N., & Scargle, J. D. 2010, *ApJ*, 717, 411
 Norris, J. P., Marani, G. F., & Bonnell, J. T. 2000, *ApJ*, 534, 248
 Paciesas, W. S., et al. 1999, *ApJS*, 122, 465
 Pélagion, A., et al. 2008, *A&A*, 491, 157
 Pellizza, L. J., et al. 2006, *A&A*, 459, L5
 Perley, D. A., et al. 2009, *AJ*, 138, 1690
 Preece, R. D., Briggs, M. S., Malozzi, R. S., Pendleton, G. N., Paciesas, W. S., & Band, D. L. 1998, *ApJ*, 506, L23
 Racusin, J. L., et al. 2008, *Nature*, 455, 183
 Rees, M. J., & Mészáros, P. 1992, *MNRAS*, 258, 41
 Roming, P. W. A., et al. 2005, *Space Sci. Rev.*, 120, 95
 Rothschild, R. E., et al. 1998, *ApJ*, 496, 538
 Sakamoto, T., et al. 2005, *ApJ*, 629, 311
 Sakamoto, T., et al. 2008, *ApJS*, 175, 179
 Sakamoto, T., et al. 2009, *ApJ*, 693, 922
 Sakamoto, T., et al. 2011, *PASJ*, 63, 215
 Salvaterra, R., et al. 2009, *Nature*, 461, 1258
 Sari, R., Piran, T., & Narayan, R. 1998, *ApJ*, 497, L17
 Sato, G., et al. 2005, *Nucl. Instrum. Methods Phys. Res. A*, 541, 372
 Scargle, J. D. 1998, *ApJ*, 504, 405
 Shirasaki, Y., et al. 2003, *PASJ*, 55, 1033
 Soderberg, A. M., et al. 2007, *ApJ*, 661, 982
 Suzuki, M., et al. 2005, *IEEE Trans. Nucl. Sci.*, 52, 1033
 Tanvir, N. R., et al. 2009, *Nature*, 461, 1254